

Design and Analysis of Centrifugal Compressors

René Van den Braembussche

ASME
PRESS

WILEY

Design and Analysis of Centrifugal Compressors

WILEY-ASME PRESS SERIES LIST

Design and Analysis of Centrifugal Compressors	Van den Braembussche	December 2018
Dynamics of Particles and Rigid Bodies – A Self-learning Approach	Daqaq	August 2018
Engineering Optimization - Applications, Methods and Analysis	Rhinehart	April 2018
Primer on Engineering Standards: Expanded Textbook Edition	Jawad	April 2018
Compact Heat Exchangers - Analysis, Design and Optimization using FEM and CFD Approach	Ranganayakulu	March 2018
Robust Adaptive Control for Fractional-Order Systems with Disturbance and Saturation	Chen	December 2017
Stress in ASME Pressure Vessels, Boilers, and Nuclear Components	Jawad	October 2017
Robot Manipulator Redundancy Resolution	Zhang	October 2017
Combined Cooling, Heating, and Power Systems: Modeling, Optimization, and Operation	Shi	August 2017
Applications of Mathematical Heat Transfer and Fluid Flow Models in Engineering and Medicine	Dorfman	February 2017
Bioprocessing Piping and Equipment Design: A Companion Guide for the ASME BPE Standard	Huitt	December 2016
Geothermal Heat Pump and Heat Engine Systems: Theory and Practice	Chiasson	September 2016
Nonlinear Regression Modeling for Engineering Applications	Rhinehart	September 2016
Fundamentals of Mechanical Vibrations	Cai	May 2016
Introduction to Dynamics and Control of Mechanical Engineering Systems	To	March 2016

Design and Analysis of Centrifugal Compressors

René Van den Braembussche

von Karman Institute
Belgium

This Work is a co-publication between ASME Press and John Wiley & Sons Ltd

WILEY



© 2019 ASME

This Work is a co-publication between ASME Press and John Wiley & Sons Ltd

All rights reserved. No part of this publication may be reproduced, stored in a retrieval system, or transmitted, in any form or by any means, electronic, mechanical, photocopying, recording or otherwise, except as permitted by law. Advice on how to obtain permission to reuse material from this title is available at <http://www.wiley.com/go/permissions>.

The right of René Van den Braembussche to be identified as the author of this work has been asserted in accordance with law.

Registered Offices

John Wiley & Sons, Inc., 111 River Street, Hoboken, NJ 07030, USA

John Wiley & Sons Ltd, The Atrium, Southern Gate, Chichester, West Sussex, PO19 8SQ, UK

Editorial Office

The Atrium, Southern Gate, Chichester, West Sussex, PO19 8SQ, UK

For details of our global editorial offices, customer services, and more information about Wiley products visit us at www.wiley.com.

Wiley also publishes its books in a variety of electronic formats and by print-on-demand. Some content that appears in standard print versions of this book may not be available in other formats.

Limit of Liability/Disclaimer of Warranty

While the publisher and authors have used their best efforts in preparing this work, they make no representations or warranties with respect to the accuracy or completeness of the contents of this work and specifically disclaim all warranties, including without limitation any implied warranties of merchantability or fitness for a particular purpose. No warranty may be created or extended by sales representatives, written sales materials or promotional statements for this work. The fact that an organization, website, or product is referred to in this work as a citation and/or potential source of further information does not mean that the publisher and authors endorse the information or services the organization, website, or product may provide or recommendations it may make. This work is sold with the understanding that the publisher is not engaged in rendering professional services. The advice and strategies contained herein may not be suitable for your situation. You should consult with a specialist where appropriate. Further, readers should be aware that websites listed in this work may have changed or disappeared between when this work was written and when it is read. Neither the publisher nor authors shall be liable for any loss of profit or any other commercial damages, including but not limited to special, incidental, consequential, or other damages.

Library of Congress Cataloging-in-Publication Data applied for

ISBN: 9781119424093

Cover Design: Wiley

Cover Images: Abstract Background © derrrek/Getty Images; Centrifugal Compressor: Courtesy of Koen Hillewaert & René Van den Braembussche

Set in 10/12pt WarnockPro by SPi Global, Chennai, India

Printed and bound by CPI Group (UK) Ltd, Croydon, CR0 4YY

10 9 8 7 6 5 4 3 2 1

to Leen

Contents

	Preface	<i>xi</i>
	Acknowledgements	<i>xiii</i>
	List of Symbols	<i>xv</i>
1	Introduction	<i>1</i>
1.1	Application of Centrifugal Compressors	<i>2</i>
1.2	Achievable Efficiency	<i>5</i>
1.3	Diabatic Flows	<i>14</i>
1.4	Transformation of Energy in Radial Compressors	<i>19</i>
1.5	Performance Map	<i>25</i>
1.5.1	Theoretical Performance Curve	<i>25</i>
1.5.2	Finite Number of Blades	<i>26</i>
1.5.3	Real Performance Curve	<i>28</i>
1.6	Degree of Reaction	<i>29</i>
1.7	Operating Conditions	<i>32</i>
2	Compressor Inlets	<i>37</i>
2.1	Inlet Guide Vanes	<i>37</i>
2.1.1	Influence of Prerotation on Pressure Ratio	<i>40</i>
2.1.2	Design of IGVs	<i>41</i>
2.2	The Inducer	<i>49</i>
2.2.1	Calculation of the Inlet	<i>50</i>
2.2.1.1	Determination of the Inducer Shroud Radius	<i>51</i>
2.2.2	Optimum Incidence Angle	<i>53</i>
2.2.3	Inducer Choking Mass Flow	<i>56</i>
3	Radial Impeller Flow Calculation	<i>61</i>
3.1	Inviscid Impeller Flow Calculation	<i>63</i>
3.1.1	Meridional Velocity Calculation	<i>63</i>
3.1.2	Blade to Blade Velocity Calculation	<i>66</i>
3.1.3	Optimal Velocity Distribution	<i>68</i>
3.2	3D Impeller Flow	<i>73</i>
3.2.1	3D Inviscid Flow	<i>73</i>
3.2.2	Boundary Layers	<i>76</i>
3.2.3	Secondary Flows	<i>78</i>
3.2.3.1	Shrouded–unshrouded	<i>82</i>
3.2.4	Full 3D Geometries	<i>84</i>

3.3	Performance Predictions	88
3.3.1	Flow in Divergent Channels	88
3.3.2	Impeller Diffusion Model	90
3.3.3	Two-zone Flow Model	94
3.3.4	Calculation of Average Flow Conditions	101
3.3.5	Influence of the Wake/Jet Velocity Ratio v on Impeller Performance	102
3.4	Slip Factor	104
3.5	Disk Friction	108
4	The Diffuser	113
4.1	Vaneless Diffusers	116
4.1.1	One-dimensional Calculation	117
4.1.2	Circumferential Distortion	122
4.1.3	Three-dimensional Flow Calculation	125
4.2	Vaned Diffusers	131
4.2.1	Curved Vane Diffusers	131
4.2.2	Channel Diffusers	135
4.2.3	The Vaneless and Semi-vaneless Space	136
4.2.4	The Diffuser Channel	143
5	Detailed Geometry Design	147
5.1	Inverse Design Methods	147
5.1.1	Analytical Inverse Design Methods	148
5.1.2	Inverse Design by CFD	152
5.2	Optimization Systems	156
5.2.1	Parameterized Definition of the Impeller Geometry	157
5.2.2	Search Mechanisms	159
5.2.2.1	Gradient Methods	160
5.2.2.2	Zero-order Search Mechanisms	161
5.2.2.3	Evolutionary Methods	161
5.2.3	Metamodel Assisted Optimization	164
5.2.4	Multiobjective and Constraint Optimization	170
5.2.4.1	Multiobjective Ranking	170
5.2.4.2	Constraints	172
5.2.4.3	Multiobjective Design of Centrifugal Impellers	173
5.2.5	Multipoint Optimization	175
5.2.5.1	Design of a Low Solidity Diffuser	175
5.2.5.2	Multipoint Impeller Design	177
5.2.6	Robust Optimization	181
6	Volutes	185
6.1	Inlet Volutes	185
6.1.1	Inlet Bends	186
6.1.2	Inlet Volutes	190
6.1.3	Vaned Inlet Volutes	193
6.1.4	Tangential Inlet Volute	194
6.2	Outlet Volutes	196
6.2.1	Volute Flow Model	196
6.2.2	Main Geometrical Parameters	197

6.2.3	Detailed 3D Flow Structure in Volutes	200
6.2.3.1	Design Mass Flow Operation	201
6.2.3.2	Lower than Design Mass Flow	204
6.2.3.3	Higher than Design Mass Flow	205
6.2.4	Central Elliptic Volutes	208
6.2.4.1	High Mass Flow Measurements	210
6.2.4.2	Medium and Low Mass Flow Measurements	215
6.2.4.3	Volute Outlet Measurements	215
6.2.5	Internal Rectangular Volutes	215
6.2.5.1	High Mass Flow Measurements	216
6.2.5.2	Medium Mass Flow Measurements	218
6.2.5.3	Low Mass Flow Measurements	219
6.2.6	Volute Cross Sectional Shape	221
6.2.7	Volute Performance	222
6.2.7.1	Experimental Results	224
6.2.7.2	Performance Predictions	225
6.2.7.3	Detailed Evaluation of Volute Loss Model	228
6.2.8	3D analysis of Volute Flow	230
6.3	Volute-diffuser Optimization	231
6.3.1	Non-axisymmetric Diffuser	233
6.3.2	Increased Diffuser Exit Width	234
7	Impeller Response to Outlet Distortion	237
7.1	Experimental Observations	238
7.2	Theoretical Predictions	242
7.2.1	1D Model	244
7.2.2	CFD: Mixing Plane Approach	245
7.2.3	3D Unsteady Flow Calculations	247
7.2.3.1	Impeller with 20 Full Blades	248
7.2.3.2	Impeller with Splitter Vanes	249
7.2.4	Inlet and Outlet Flow Distortion	249
7.2.4.1	Parametric Study	253
7.2.5	Frozen Rotor Approach	254
7.3	Radial Forces	258
7.3.1	Experimental Observations	258
7.3.2	Computation of Radial Forces	263
7.4	Off-design Performance Prediction	267
7.4.1	Impeller Response Model	268
7.4.2	Diffuser Response Model	269
7.4.3	Volute Flow Calculation	269
7.4.4	Impeller Outlet Pressure Distribution	272
7.4.5	Evaluation and Conclusion	273
8	Stability and Range	275
8.1	Distinction Between Different Types of Rotating Stall	276
8.2	Vaneless Diffuser Rotating Stall	280
8.2.1	Theoretical Stability Calculation	284
8.2.2	Comparison with Experiments	287
8.2.3	Influence of the Diffuser Inlet Shape and Pinching	289

8.3	Abrupt Impeller Rotating Stall	296
8.3.1	Theoretical Prediction Models	297
8.3.2	Comparison with Experimental Results	300
8.4	Progressive Impeller Rotating Stall	301
8.4.1	Experimental Observations	301
8.5	Vaned Diffuser Rotating Stall	307
8.5.1	Return Channel Rotating Stall	314
8.6	Surge	314
8.6.1	Lumped Parameter Surge Model	316
8.6.2	Mild Versus Deep Surge	321
8.6.3	An Alternative Surge Prediction Model	325
9	Operating Range	329
9.1	Active Surge Control	330
9.1.1	Throttle Valve Control	331
9.1.2	Variable Plenum Control	333
9.1.3	Active Magnetic Bearings	335
9.1.4	Close-coupled Resistance	336
9.2	Bypass Valves	337
9.3	Increased Impeller Stability	340
9.3.1	Dual Entry Compressors	342
9.3.2	Casing Treatment	344
9.4	Enhanced Vaned Diffuser Stability	347
9.5	Impeller–diffuser Matching	351
9.6	Enhanced Vaneless Diffuser Stability	354
9.6.1	Low Solidity Vaned Diffusers	356
9.6.2	Half-height Vanes	359
9.6.3	Rotating Vaneless Diffusers	359
	Bibliography	363
	Index	385

Preface

The growing awareness of the need for energy savings and the increase of efficiency of centrifugal compressors over the last decades has resulted in an increasing field of applications. The compactness, small weight and simplicity of the components allow an efficient replacement of multistage axial compressors by a single stage radial one. The absence of mechanical friction, lower life time cost and high reliability makes centrifugal compressors also superior to reciprocal ones. All this has led to a revival of centrifugal compressor research.

Centrifugal compressors are very different from axial ones and require a specific approach. This book intends to respond to that. Extensive reference is made to the experimental results and analytical flow models that have been developed during the last (pre-computer) century and published in the open literature. This is complemented by the research conducted in the context of the PhD. thesis of Drs. Paul Frigne, George Verdonk, Marios Sideris, Antonios Fatsis, Erkan Ayder, Koen Hillewaert, Alain Demeulenaere, Olivier Léonard, Stephane Pierret, Tom Verstraete, Alberto Di Sante and the research projects of the many Master students that I had the pleasure to supervise.

The book does not provide the recipe to design “the optimal compressor” but rather insight into the flow structure. The purpose is to help remediate problems, finding a compromise between the different design targets and restrictions and help for a better reading and hence a more efficient use of Navier-Stokes results.

Numerical techniques are not described in detail but attention is given to their application, in particular to the correct operating conditions and restrictions of the different approaches and to their use in the modern computational design and optimization techniques developed during the last two decades.

The book is based on the “Advanced Course Centrifugal Compressors” that is taught by the author in the “Research Master Program” at the von Karman Institute. It intends to be a reference for engineers involved in the design and analysis of centrifugal compressors as well as teachers and students specializing in this field.

I am indebted to my former colleagues at the von Karman Institute, Profs. Frans Breugelmans, Claus Sieverding, Tony Arts and my successor Tom Verstraete. Working with them has been a very enriching and motivating experience. Thanks also to Dr. Z. Alsalihi and ir. J. Prinsier for the many years of fruitful collaboration and CFD support including the preparation of figures, and to the VKI librarians Christelle De Beer and Evelyne Crochard for their logistic help in preparing this book.

This book would not have been realized without the understanding, encouragement and unlimited support of Leen, my wife and soul-mate for more than fifty years. Special thanks for that.

Alseberg, February 25, 2018

*René Van den Braembussche,
Hon. Professor von Karman Institute*

Acknowledgements

The author wishes to thank the Forschungsvereinigung Verbrennungskraftmaschinen (FVV) for permission to include results in this book and in particular the members of the working group Vorleitschaufeln for the many fruitful discussions.

Permissions from the following to reproduce copyrighted material is gratefully recognized:

The American Society of Mechanical Engineers for: figs. 5 and 6 from Abdelhamid (1980) as fig. 8.33, fig. 3 from Abdelhamid (1982) as fig. 9.39, figs. 2 and 5 from Abdelhamid (1987) as fig. 9.40, fig. 9b from Abdelwahab (2010) as fig. 7.8, figs. 4 and 6 from Agostinelli et al. (1960) as figs. 7.25 and 7.26, figs. 8 and 9 from Amann et al. (1975) as fig. 9.27, figs. 15 and 16 from Ariga et al. (1987) as fig. 8.43, fig. 16 from Arnulfi et al. (1999b) as fig. 9.7, figs. 1 and 9 from Baljé (1970) as fig. 3.15, fig. 3 from Bhinder and Ingham (1974) as fig. 3.12, fig. 6b from Bonaiuti et al. (2002) as fig. 4.27, fig. 11b from Bowermann and Acosta (1957) as fig. 6.22, fig. 1 from Casey (1985) as fig. 1.20, figs. 2 and 13 from Chen and Lei (2013) as fig. 9.23, figs. 7 and 14 from Chen et al. (1993) as fig. 9.39, figs. 1 and 2 from Childs and Noronha (1999) as fig. 1.17, fig. 8d from Conrad et al. (1980) as fig. 4.36, fig. 6 from Davis and Dussourd (1970) as fig. 3.2, fig. 7 from Dean and Senoo (1960) as fig. 4.13, fig. 6 from Dean and Young (1977) as fig. 8.55, fig. 3 from Dickmann et al. (2005) as fig. 9.22, fig. 3 from Dussourd and Putman (1960) as fig. 9.20, figs. 5, 11, and 12 from Dussourd et al. (1977) as figs. 9.10 and 9.9, figs. 7 to 11 from Eckardt (1976) as figs. 3.34 and 8.60, fig. 9 from Elder and Gill (1984) as fig. 8.47, figs. 10, 11, 13, 15, and 17 from Ellis (1964) as figs. 3.16, 4.20, and 4.21, figs. 7 and 96 from Everitt and Spakovszky (2013) as figs. 7.11 and 8.45, fig. 8 from Fink et al. (1992) as fig. 8.64, figs. 4, 10, and 11 from Flathers et al. (1996) as figs. 6.10 and 6.14, figs. 16 and 17 from Flynn Weber (1979) as fig. 9.16, fig. 4 from Fowler (1966) as fig. 1.10, fig. 7b from Greitzer (1976) as fig. 8.67, fig. 16 from Gyarmathy (1996) as figs. 8.50 and 8.51, fig. 3 from Hayami et al. (1990) as fig. 9.42, fig. 11 from Hunziker and Gyarmathy (1994) as fig. 8.44, figs. 12 and 13 from Ishida et al. (2000) as fig. 9.38, figs. 8 and 14 from Jansen (1964b) as fig. 8.11, fig. 2 from Kammer and Rautenberg (1986) as fig. 8.61, figs. 4 and 6 from Kang Jeong-seek et al. (2000) as fig. 4.32, fig. 9 from Kinoshita and Senoo (1985) as fig. 8.14, figs. 5 and 10 from Koch et al. (1995) as figs. 6.12 and 6.13, fig. 1 from Krain (1981) as fig. 4.2, fig. 12 from Kramer et al. (1960) as fig. 3.11, figs. 4 and 6 from Lennemann and Howard (1970) as figs. 8.1 and 8.37, figs. 7.1 and 7.2 from Lüdtke (1983) as fig. 9.37, figs. 16 and 26 from Lüdtke (1985) as figs. 6.16, 6.8, and 6.9, figs. 15 and 16 from Mishina and Gyobu (1978) as figs. 6.20 and 6.21, figs. 6a and 9 from Mizuki et al. (1978) as figs. 8.34 and 8.38, fig. 5 from Morris et al. (1972) as fig. 2.3, figs. 1b, 2c, and 3c from Mukkavilli et al. (2002) as figs. 9.43, 9.44, and 9.45, fig. 3 from Nece and Daily (1960) as fig. 3.53, fig. 4 from Pampreen (1989) as fig. 4.25, figs. 4b and 4d from Reneau et al. (1967) as fig. 4.41, fig. 10 from Rodgers (1968) as fig. 9.33, figs. 2b and 5 from Rodgers (1977) as figs. 2.10 and 9.15, figs. 5 and 6 from Rodgers (1978) as fig. 8.40, fig. 3 from Rodgers (1962) as fig. 2.23, fig. 4 from Rodgers (1998) as fig. 2.31, fig. 7 from Rodgers (1991) as fig. 1.15, fig. 2 from Rodgers (1980), as fig. 1.14, figs. 4, 14, and 17 from Sapiro (1983) as figs.

9.46 and 9.47, fig. 1 from Strub et al. (1987) as fig. 1.16, fig. 1 from Rothe and Runstadler (1978) as fig. 8.63, figs. 5, 23, 25, 26, and 27 from Runstadler Dean (1969) as figs. 4.1 and 4.42, figs. 4 and 2 from Salvage (1998) as figs. 4.39 and 9.35, fig. 12 from Senoo Ishida (1975) as fig. 4.12, fig. 1 from Senoo et al. (1977) as fig. 4.16, figs. 7, 4a, 5a, and 6 from Senoo and Kinoshita (1977) as figs. 8.15 to 8.19, fig. 6 from Senoo and Kinoshita (1978) as fig. 8.18, fig. 3 from Senoo et al. (1983a) as fig. 4.26, figs. 7 and 13 from Simon et al. (1986) as figs. 2.6 and 9.34, fig. 1 from Simon et al. (1993) as fig. 9.5, fig. 15 from Sugimura et al. (2008) as fig. 5.30, fig. 19 from Tamaki et al. (2012) as fig. 9.25, figs. 6 and 7 from Toyama et al. (1977) as figs. 8.65 and 8.66, fig. 11 from Trébinjac et al. (2008) as fig. 4.31, fig. 8 and 5b from Tsujimoto et al. 1994 as figs. 8.35 and 8.9, fig. 126 from Wiesner (1967) as fig. 3.49, figs. 3 and 15 from Yoon et al. (2012) as fig. 9.8, fig. 4 from Yoshida et al. (1991) as fig. 9.29, figs. 7 and 8 from Yoshinaga et al. (1985) as fig. 9.45, figs. 5b and 8a and c from Tsujimoto et al. (1994) as figs. 8.9 and 8.35, fig. 7 from Kosuge et al. (1982) as fig. 8.41, fig. 14 from Marsan et al. (2012) as fig. 9.30.

ConceptsNREC for: fig. 1.7 from Japikse and Baines (1994) as fig. 1.13, fig. 6.9 from Japikse (1996) as fig. 8.42.

Dr. Heinrich for fig. 11 from Heinrich and Schwarze (2017) as fig. 6.59.

Gas Turbine Society of Japan for: figs. 2 and 4 from Krain at al. (2007) as fig. 4.29.

Institution of Mechanical Engineering for: figs. 14 and 15 from Japikse (1982) as fig. 6.62, fig. 1 from Sideris et al. (1986) as fig. 4.2.

International Association of Hydraulic Research for: figs. 2, 3, 4, 5, 6, and 7 from Matthias (1966) as fig. 6.4, fig. 1 from Rebernik (1972) as fig. 4.19.

Japan Society of Mechanical Engineering for: fig. 11 from Hasegawa et al. (1990) as fig. 7.23, fig. 13 from Aoki et al. (1984) as fig. 7.27, figs. 13, 6, and 7 from Nishida et al. (1991) as figs. 8.27 and 9.41, figs. 2 and 8 from Nishida et al. (1988) as figs. 8.21 and 8.23, figs. 2, 4, 5, 6, 7, 11, and 13 from Kobayashi et al. (1990) as figs. 8.22, 8.23, 8.24, 8.25, and 8.28.

J. Wiley and Sons for: figs. 6.66 and 5.133 from Baljé (1981) as figs. 9.35 and 2.24, figs. 2.12 and 2.15 from Neumann (1991) as figs. 6.11 and 6.15.

NATO Science and Technology Organization for: fig. 6a from Benvenuti et al. (1980) as fig. 2.27, fig. 7 from Walitt (1980) as fig. 3.1, fig. 3c2 from Poulain and Janssens (1980) as fig. 3.33b, figs. 14 and 15 from Vavra (1970) as figs. 3.37 and 3.54, figs. 3b, 10, 4, and 112 from Jansen et al. (1980) as figs. 9.21 and 9.26, fig. 1a from Japikse (1980) as fig. 8.48, fig. 13 from Vinau et al. (1987) as fig. 9.31, figs. 25 and 37 from Kenny (1970) as figs. 4.33 and 8.46.

Prof. M. Rautenberg for: figs. 8, 9, 10, and 11 from Rautenberg et al. (1983) as figs. 1.24a and 1.24b.

Sage Publications for: fig. 8 from Casey and Robinson (2011) as fig. 1.18, fig. 22 from Peck (1951) as fig. 6.57.

Solar Turbines Incorporated for: figs. 7, 15, and 16 from White and Kurz (2006) as figs. 9.13 and 9.14.

Springer Verlag for fig. 6.16.6 from Traupel (1966) as fig. 3.50, fig. 381 from Eckert and Schnell (1961) as fig. 3.51, figs. 12, 15, and 17 from Pfau (1967) as fig. 7.2.

The Academic Computer center in Gdansk TASC for: fig. 9 from Dick et al. (2001) as fig. 7.21.

Toyota Central Laboratory for: fig. 4 from Uchida et al. (1987) as fig. 7.3.

Tsukasa Yoshinaka for: figs. 3, 4, 5, and 9 from Yoshinaka (1977) as figs. 8.68, 8.69, 8.70, and 8.71.

von Karman Institute for: figs. 3, 15, and 17 from Benvenuti (1977) as figs. 1.3 and 1.4, fig. 4 from Breugelmans (1972) as fig. 2.4, figs. 2, 3b, 4, 7, and 25 from Dean (1972) as figs. 1.1, 2.1, 3.41, 3.42, and 4.43, fig. 11 from Senoo (1984) as fig. 4.17, figs. 20 and 22 from Stiefel (1972) as fig. 6.19, fig. 26 from Schmallfuss (1972) as fig. 9.17.

List of Symbols

A	cross section area
$A(U(\vec{X}), \vec{X})$	performance constraint function
AIRS	abrupt impeller rotating stall
AR	area ratio
AS	aspect ratio (b/O_{th})
a	speed of sound
\vec{a}	acceleration
A_σ	real part of growth rate S
b	impeller outlet or diffuser width
B^2	Greitzer B^2 factor (Equation 8.43)
B_f	distortion factor
bl	relative blockage
c	chord length
C	impeller outlet jet flow area at zero wake velocity
C_d	dissipation coefficient
C_f	Darcy friction coefficient
CDF	cumulative density function
CFD	computational fluid dynamics
CFL	Courant-Friedrichs-Lewy
C_m	momentum or torque coefficient
C_M	jet-wake friction coefficient
CP	static pressure rise coefficient
C_p	specific heat coefficient
D	diameter
DH	hydraulic diameter
DOE	design of experiment
DR	diffusion ratio (W_1/W_{SEP})
dS	control surface
EL	equivalent channel length
ESD	emergency shut down
EM	emergency shut-off valve
f	frequency of unsteadiness
F	force
FEA	finite element stress analysis
g	gravity acceleration
G	controller gain
$G_k(\vec{X})$	geometric constraint function

GPM	gallons per minute
h	static enthalpy
h_b	blade to blade distance
H	total enthalpy
	manometric height
i	incidence
J	moment of inertia
k_s	equivalent sand grain size of roughness
K	radial force coefficient (eqn. 7.14)
k_b	blade blockage
L	length of channel
LH	hydraulic length
LSD	low solidity diffuser
LWR	length over width ratio
m	meridional distance
\dot{m}	mass flow
M	Mach number
Mo	momentum or torque
M_R	radial momentum
M_u	tangential momentum
M_x	axial momentum
NACA	National Advisory Committee for Aerodynamics
NS	specific speed
NUEL	number of circumferential positions
n	distance perpendicular to axisymmetric streamsurface
n_D	number of design parameters
N	number of rotations (RPM)
	number of individuals in a population
NPSHR	net positive suction head required
O	opening or throat width
$OF(U(\vec{X}), \vec{X})$	objective function
P	pressure
	amplitude of power spectrum
	penalty
PDF	probability density function
PIRS	progressive impeller rotating stall
P_w	power (W)
\dot{Q}	volumetric flow
q	heat flux per unit mass
Q	heat flux (W)
	dynamic pressure ($P^o - P$)
R	radius measured from impeller axis
$R(U(\vec{X}), \vec{X})$	performance evaluator
r	radius measured from the volute cross section center
	degree of reaction
\mathfrak{R}	curvature radius
	diffuser inlet round-off radius
Re	Reynolds number
R_f	relaxation factor

R_G	gas constant
RHS	right hand side
Ro	rothalpy
RPM	rotations per minute
RV	hub/shroud radius ratio (R_{1H}/R_{1S})
s	distance along streamline
S	surface
	exponential growth rate of perturbation
	entropy
S_r	acoustic Strouhal number
S_x	axial gap between impeller backplate and casing
t	time
	pitch
T	temperature
u	non-dimensionalized meridional length
U	peripheral velocity
$U(\vec{X})$	output of performance evaluator
v	absolute velocity in the boundary layer
V	free stream absolute velocity
VDRS	vaneless diffuser rotating stall
\mathcal{V}_c	compressor volume
\mathcal{V}_p	plenum volume
w	relative velocity in the boundary layer
W	free stream relative velocity
x	axial or longitudinal distance
\vec{X}	geometry
y	distance in pitchwise direction
	direction perpendicular to x and z
Z	number of blades or vanes
	controller transfer function
Z_p, Z_u	parameters defining diffuser inlet conditions (Equations 8.9 and 8.10)
z	direction perpendicular to x and y
α	absolute flow angle measured from meridional plane
β	relative flow angle measured from meridional plane
β_σ	phase shift of controller
γ	angle between meridional streamsurface and axial direction
δ	boundary layer thickness
	ratio of inlet pressures (Equation 1.106)
δ_{cl}	impeller - shroud clearance gap
δ_{bl}	blade thickness perpendicular to camber
ϵ	skewness angle between wall streamline and main flow direction
e	relative wake width
ϵ_{kb}	relative blade blockage
η	isentropic efficiency
η_W	wheel diffusion efficiency (Equation 3.40)
θ	angular coordinate (measured from the tongue)
	half diffuser opening angle
	ratio of inlet total temperatures (Equation 1.103)
κ	isentropic exponent

λ	number of stall cells or rotating waves ratio of wake mass flow/total mass flow
μ	work reduction factor dynamic viscosity
ν	wake/jet velocity ratio kinematic viscosity μ/ρ
ω	total pressure loss coefficient
Ω	impeller rotational speed (rad/sec)
Ω_R	reduced frequency (Equation 7.1)
ω_m	m^{th} modal frequency of the impeller
ω_s	streamwise vorticity
ω_σ	rotational speed of stall cell imaginary part of S
π	pressure ratio
ϕ	flow coefficient (V_m/U)
ψ	non dimensional pressure rise coefficient
Ψ	streamfunction
ρ	density
σ	slip factor solidity (chord/pitch) stress (MPa)
τ	time for one impeller rotation period of perturbation shear stress
∇	$\vec{i}_x \frac{\partial}{\partial x} + \vec{i}_y \frac{\partial}{\partial y} + \vec{i}_z \frac{\partial}{\partial z}$
∇	vector product
∇^2	Laplace operator

Subscripts

0	upstream of IGW or inlet volute
01	downstream IGW
1	impeller inlet
2	impeller outlet
3	vaned diffuser leading edge
4	diffuser outlet
5	volute exit
6	compressor outlet - return channel exit
11	at the inner radius of the impeller backplate
<i>a</i>	absolute frame of reference
<i>ad</i>	adiabatic
<i>b</i>	in blade to blade direction
<i>bl</i>	of the blade
<i>b2</i>	based on the impeller outlet width
<i>C</i>	of the compressor
<i>c</i>	critical value
	at center of volute cross section
<i>ce</i>	due to centrifugal forces
<i>ch</i>	at choking

<i>cl</i>	due to clearance
<i>Cor</i>	due to Coriolis forces
<i>curv</i>	due to curvature
<i>D</i>	of the diffuser deterministic solution
<i>d</i>	downstream
<i>des</i>	design value
<i>dia</i>	diabatic
<i>EC</i>	of the exit cone
<i>F</i>	of the force
<i>fl</i>	of the flow
<i>fr</i>	due to friction
<i>H</i>	at the hub
<i>i, j, k</i>	indices in meridional, tangential and normal direction
<i>IGV</i>	inlet guide vane setting angle
<i>inc</i>	incompressible due to incidence
<i>inl</i>	at the inlet
<i>iw</i>	at the inner wall
<i>j</i>	in the jet index of circumferential position
<i>kb</i>	due to blade blockage
<i>LE</i>	leading edge value
<i>m</i>	meridional component
<i>max</i>	maximum value
<i>mech</i>	mechanical
<i>min</i>	minimum value
<i>MC</i>	corresponding to remaining swirl
<i>MVDL</i>	due to meridional velocity dump losses
<i>n</i>	normal component
<i>N</i>	nominal value
<i>o</i>	at the outlet
<i>opt</i>	optimum value
<i>ow</i>	at the outer wall
<i>p</i>	of the pipe polytropic
<i>P</i>	due to pressure of the plenum
<i>PS</i>	on the pressure side
<i>r</i>	of the rotor (relative frame)
<i>R</i>	radial component at resonance robust solution
<i>ref</i>	reference value, reference gas
<i>ret</i>	at return flow
<i>Ro</i>	corresponding to rothalpy / corrected for rotation
<i>s</i>	streamwise component
<i>S</i>	at the shroud swirl component

SS	on the suction side
$S - S$	static to static
SEP	at separation point
T	trough flow or tangential component of the throttle device
TE	trailing edge value
th	at the throat section
$T - S$	total to static
$T - T$	total to total
$TVDL$	due to tangential velocity dump losses
u	peripheral component upstream
un	uncontrolled
V	based on absolute velocity
w	in the wake on the wall
W	based on relative velocity
x	axial component
∞	free stream value at high Reynolds number

Superscripts

i	isentropic
k	number of the time step
nr	non rotating
o	stagnation conditions
t	at next time step or generation
\wedge	perturbation component
\sim	average
\rightarrow	vector
∞	assuming an infinite number of blades
\star	target value
$'$	$\partial./\partial\phi$

1

Introduction

A radial compressor can be divided into different parts, as shown in Figure 1.1. The flow is aspirated from the **inlet plenum** and after being deflected by the **inlet guide vanes** (IGV), it enters the **inducer**. From there on the flow is decelerated and turned into the axial and radial directions before leaving the impeller in the **exducer**. The presence of a radial velocity component is responsible for Coriolis forces, which, together with the blade curvature effect, tends to stabilize the boundary layer at the shroud and suction side of the inducer (Johnston 1974; Koyama et al. 1978). The boundary layer becomes less turbulent and will more easily separate under the influence of an adverse pressure gradient.

Two different flow zones can be observed inside the impeller resulting from flow separation and secondary flows (Carrad 1923; Dean 1972):

- A highly energetic zone with a high relative Mach number, commonly called the **jet**. The flow in this zone is considered quasi isentropic.
- A lower energetic zone with a low relative Mach number where the flow is highly influenced by losses. This zone, commonly called the **wake**, is fed by the boundary layers and influenced by secondary flows.

After leaving the impeller, rapid mixing takes place between the two zones due to the difference in angular momentum (**mixing region**). This intensive energy exchange results in a fast uniformization of the flow.

The flow is further decelerated by an area increase corresponding to the radius increase of the **vaneless diffuser** and influenced by friction on the lateral walls.

In case of a **vaned diffuser**, the flow, after a short vaneless space, enters the **semi-vaneless space**, i.e. the diffuser entry region between the leading edge and the throat section where a rapid adjustment rearranges the isobar pattern from nearly circumferential to perpendicular to the main flow direction. If the Mach number is higher than one, a shock system may decelerate the flow such that the **throat section** becomes subsonic.

A further decrease in the velocity in the divergent **diffuser channel** downstream of the throat realizes an additional increase in the static pressure. Depending on the throat flow conditions, the boundary layers in this channel will thicken or even separate, which limits the static pressure rise.

The flow may exit the compressor by a **volute** or plenum, or can be guided into the next stage by a **return channel**.

The following chapters describe the flow in the different parts (IGV, impeller, diffuser, etc.) together with the equations governing the flow in these components. A first objective is to provide insight into the flow structure to allow a better understanding of numerical and experimental results. A second objective is the characterization of the compressor components based on a limited number of geometrical parameters, experimental correlations, and flow

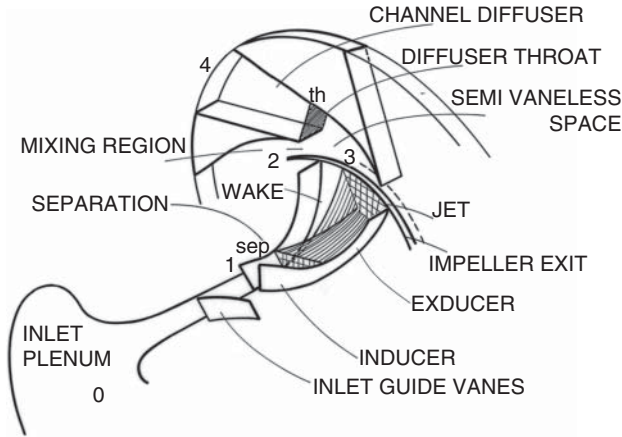


Figure 1.1 Schematic view of the radial compressor components and flow (from Dean 1972).

parameters such as the diffusion ratio (DR), the jet wake mass flow ratio (λ) for the impeller flow, the pressure recovery (CP) for the diffuser, etc.

The ultimate purpose is to provide input for the design of compressors that better satisfy the design requirements in terms of pressure ratio, efficiency, mass flow, and stable operating range.

1.1 Application of Centrifugal Compressors

Experience has shown that the specific speed NS is a valuable parameter in the selection of the type of compressor (axial, centrifugal or volumetric) that is best suited for a given application.

The specific speed is defined by

$$NS = \frac{RPM \sqrt{\dot{Q}}}{\Delta H^{3/4}} \quad (1.1)$$

This is a non-dimensional parameter only if coherent units are used (m^3/s for the volume flow \dot{Q} , m^2/s^2 for the enthalpy rise ΔH). However, a commonly used definition of specific speed for compressors

$$NS_C = \frac{RPM \sqrt{ft^3/s}}{ft^{3/4}} \quad (1.2)$$

does not use SI units and is not non-dimensional.

A common definition for pumps is

$$NS_P = \frac{RPM \sqrt{GPM}}{ft^{3/4}} \quad (1.3)$$

where GPM = US gallon/min and the manometric head is in ft.

The following definitions in SI units are non-dimensional:

$$NS_1 = \frac{\Omega \sqrt{m^3/s}}{\Delta H^{3/4}} \quad \text{or} \quad NS_2 = \frac{RPS \sqrt{m^3/s}}{\Delta H^{3/4}} \quad (1.4)$$

Previous definitions are linked by:

$$NS_C = 129.01NS_1 \quad NS_C = 2\pi 129.01NS_2 \quad NS_p = 21.22NS_C \quad (1.5)$$

Radial compressors can achieve high pressure ratios and the inlet volume flow can be very different from the one at the outlet. We should therefore verify which one of the two has been used in the definition of NS . Rodgers (1980) proposes using an average value of the inlet and outlet volumetric flow:

$$\tilde{Q} = \frac{\dot{Q}_1 + \dot{Q}_6}{2}$$

The variation of efficiency as a function of specific speed for axial, centrifugal, and volumetric compressors is shown in Figure 1.2. Test results for numerous compressors lie within the shaded areas and the full lines envelop the data corresponding to the different types. The meridional cross section of the corresponding type of compressor geometry is shown on top. The limiting curves on the figure intend only to show the trend in compressor efficiency as a function of specific speed. They should not be used for prediction purposes because the information dates from a period when the flow in radial impellers was not yet fully understood (Baljé 1961). Great improvements have been made since then, thanks to the information obtained by CFD and optical measurement techniques. More recent results are shown in Figure 1.14.

Centrifugal compressors can also be designed for specific speed values away from the optimum indicated on Figure 1.2 but this does not facilitate the job. Positive displacement (volumetric) compressors are often replaced by less efficient very low specific speed centrifugal compressors for operational and maintenance reasons.

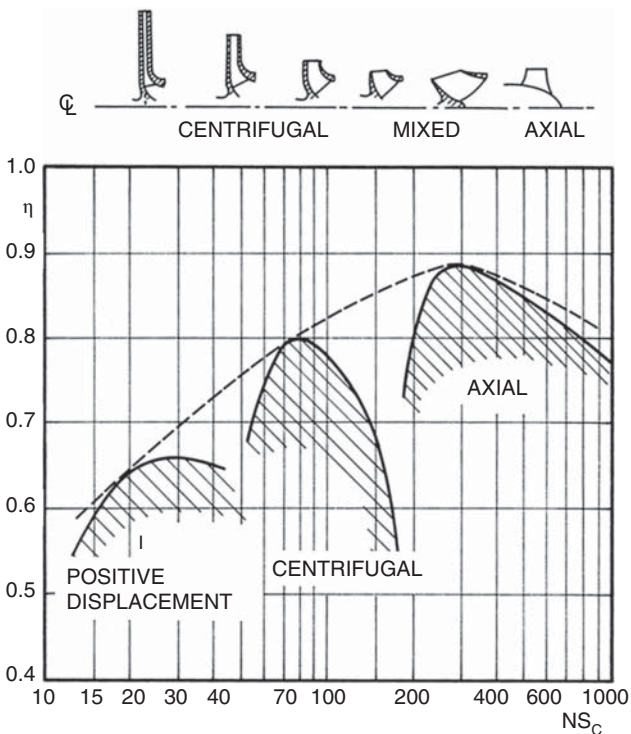


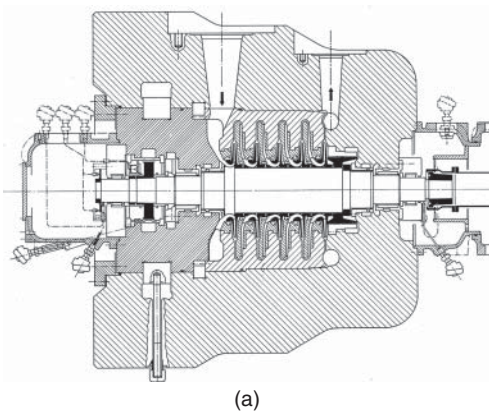
Figure 1.2 Variation of efficiency and geometry with specific speed.



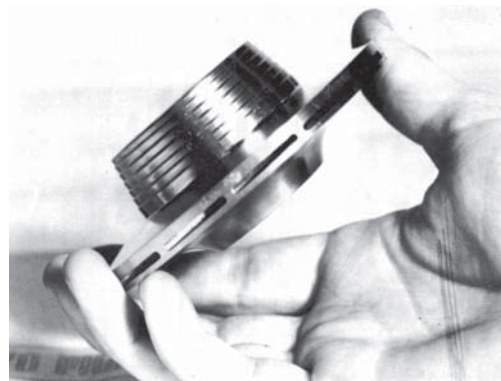
Figure 1.3 Industrial centrifugal impellers (from Benvenuti 1977).

Centrifugal compressors are used at lower NS than axial compressors. The low NS may result from:

- operation at low RPM: this is often the case with industrial compressors (Figure 1.3) for reasons of maximizing lifetime
- small volume flow as occurring in last stages (Figure 1.4a) of multistage industrial compressors (Figure 1.4b)
- a high pressure ratio per stage in combination with a small volume flow (Figure 1.5) or even large volume flow in combination with very large pressure ratios (Figure 1.6) as occurs in turbochargers
- a high pressure ratio and small volume flow as in small gas turbines for automotive applications (Figure 1.7), in the last compressor stages of small gas turbines, turboprop or jet engines (Figure 1.8), and in micro gas turbines (Figure 1.9).



(a)



(b)

Figure 1.4 (a) Last corps of a high pressure industrial centrifugal compressor with (b) very low specific speed impeller (from Benvenuti 1977).

Figure 1.5 Cross section of a turbocharger (courtesy of MHI).

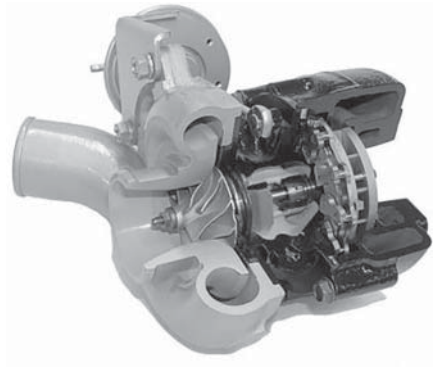


Figure 1.6 Large turbocharger for ship diesel engine (courtesy of ABB Turbo Systems Ltd).

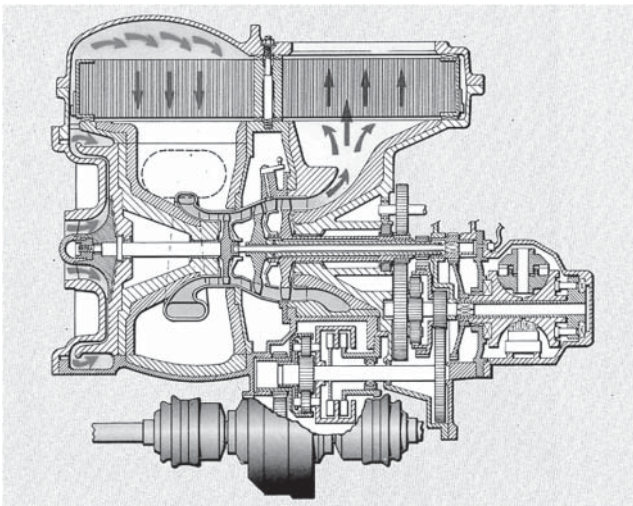
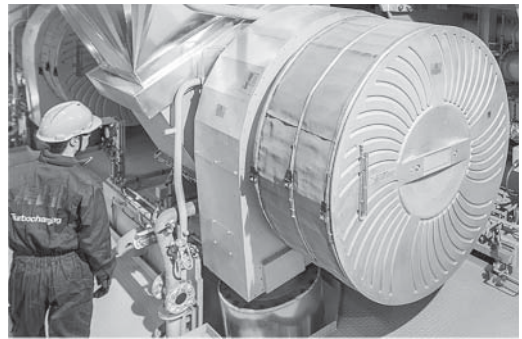


Figure 1.7 Layout of a gas turbine for automotive applications (courtesy of Volvo Group Trucks Technology).

1.2 Achievable Efficiency

Figure 1.2 shows a much lower maximum efficiency for radial compressors than for axial ones. As already mentioned, this figure dates from the time that the flow in radial compressors was not yet well understood and they were designed by simple rules and intuition, complemented by analytical considerations and empiricism. The relative flow in radial compressors being

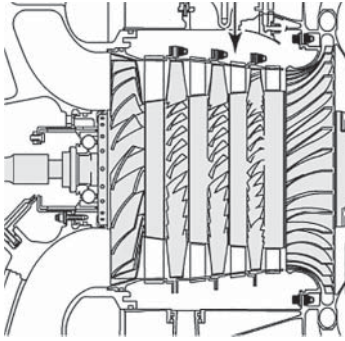
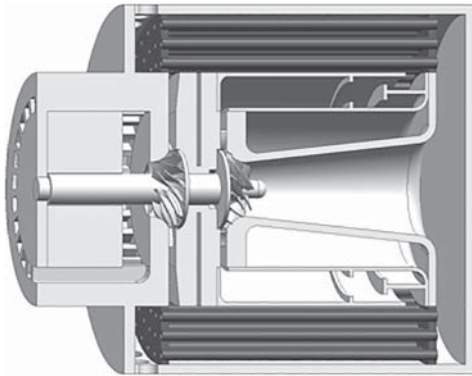


Figure 1.8 Compressor of a turboprop engine with radial endstage (courtesy of Pratt & Whitney Canada Corp.).



(a)



(b)

Figure 1.9 (a) Cross section of a micro gas turbine and (b) view of generator and impellers (diameter of 20 mm).

rotational, it is not possible to study the flow experimentally in a stationary (non-rotating) facility, as was done by NACA for axial compressors (Herrig et al. 1957). The heroic experimental campaign of Fowler (1966, 1968) was the start of a better understanding of the real three-dimensional (3D) flow in radial impellers (Figure 1.10). It has been complemented by advanced optical measurements (Eckardt 1976).

Before starting to discuss the maximum value of achievable efficiencies, one should first clarify the different definitions of efficiency (Figure 1.11). The temperature and enthalpy are related by the specific heat coefficient C_p . The following theoretical considerations assume constant C_p . Hence the T, S diagram is interchangeable with the H, S diagram.

The flow entering the compressor has a static temperature T_1 and a total temperature T_1^o . The difference is the kinetic energy at the impeller inlet $V_1^2/2C_p$. The static pressure at the impeller exit P_2 is achieved with a static temperature rise to T_2 and a total temperature T_2^o . An isentropic compression to the same static pressure would have resulted in an outlet static temperature T_2^i and total temperature $T_2^{o,i}$.

Considering only the static pressure at the *impeller* exit (2), the ratio of the minimum required energy over the real added one is called total to static efficiency, and is defined by:

$$\eta_{2,T-S} = \frac{T_2^i - T_1^o}{T_2^o - T_1^o} = \frac{(P_2/P_1^o)^{\frac{\kappa-1}{\kappa}} - 1}{(T_2^o - T_1^o)/T_1^o} \quad (1.6)$$

In most cases this will be a low value because in this definition the kinetic energy at the impeller exit is considered lost or useless.

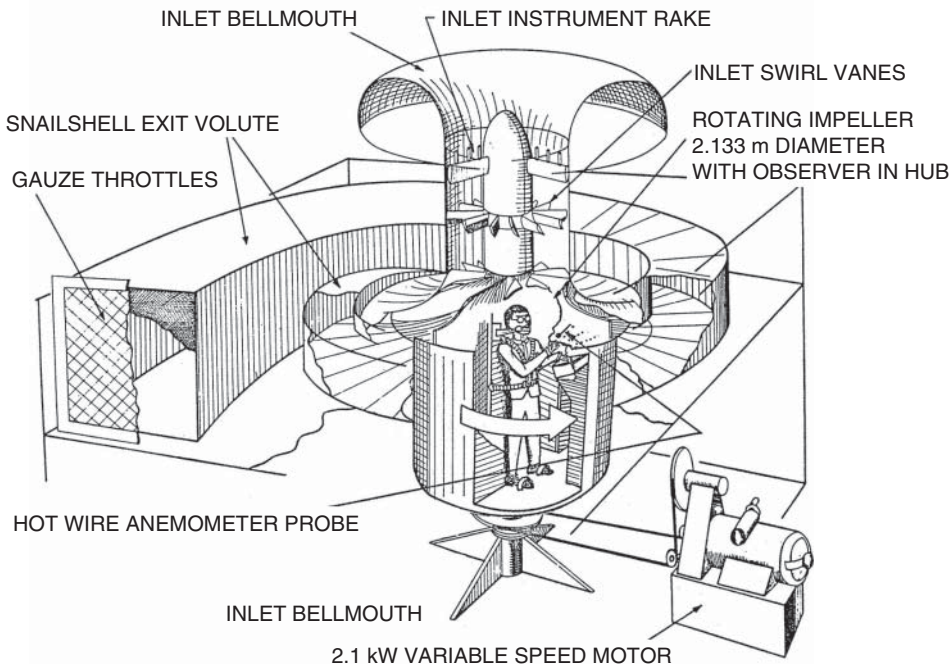
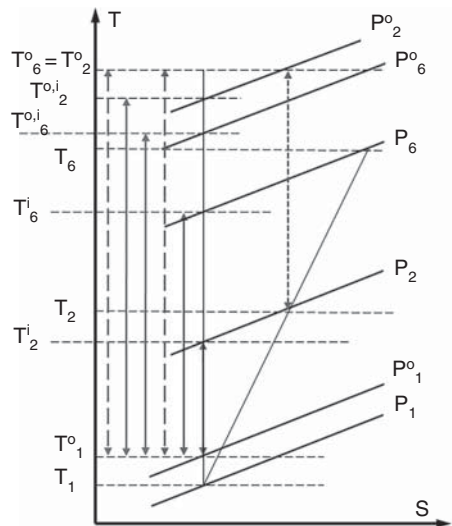


Figure 1.10 Measurements of the relative flow in a rotating impeller (from Fowler 1966).

Figure 1.11 Definition of efficiencies.



The total to total efficiency, defined by:

$$\eta_{2,T-T} = \frac{T_2^{o,i} - T_1^o}{T_2^o - T_1^o} = \frac{(P_2^o/P_1^o)^{\frac{\kappa-1}{\kappa}} - 1}{(T_2^o - T_1^o)/T_1^o} \quad (1.7)$$

is much higher (Figure 1.11) because it considers that the kinetic energy at the impeller exit ($V_2^2 = 2C_p(T_2^o - T_2)$) is also useful.

Considering the static and total flow conditions at the *compressor* exit (6), the previous definitions become:

$$\eta_{6,T-S} = \frac{T_6^i - T_1^o}{T_6^o - T_1^o} = \frac{(P_6/P_1^o)^{\frac{\kappa-1}{\kappa}} - 1}{(T_6^o - T_1^o)/T_1^o} \tag{1.8}$$

$$\eta_{6,T-T} = \frac{T_6^{o,i} - T_1^o}{T_6^o - T_1^o} = \frac{(P_6^o/P_1^o)^{\frac{\kappa-1}{\kappa}} - 1}{(T_6^o - T_1^o)/T_1^o} \tag{1.9}$$

The total to static efficiency is now much larger than at the impeller exit because part of the kinetic energy available at the impeller exit has been transformed into pressure by the stator/diffuser.

However, the total to total efficiency at the compressor exit is lower than at the impeller exit because the $T_6^{o,i}$ is smaller than $T_2^{o,i}$, due to the stator/diffuser losses. The total temperature rise $T_6^o - T_1^o = T_2^o - T_1^o$ because no energy is added in an adiabatic non-rotating diffuser. When comparing the efficiency of different compressors one should therefore verify if the same definition of the efficiency has been used.

The polytropic efficiency is commonly used for multistage and high pressure ratio compressors to correct for the divergence of the iso-pressure lines. Polytropic efficiency compares the real enthalpy rise with the hypothetical one of an infinite number of compressor stages each with an infinitesimal small pressure rise producing the same overall pressure and temperature rise of the complete compressor (Figure 1.12). Hence:

$$\eta_p = \frac{\sum \Delta T^i}{\sum \Delta T} = \frac{\sum \Delta T^i}{T_n - T_1} > \frac{T_n^i - T_1}{T_n - T_1} = \eta \tag{1.10}$$

This is therefore called small stage efficiency and can also be written as:

$$\eta_p = \frac{\kappa - 1}{\kappa} \frac{\ln(\frac{P_n}{P_1})}{\ln(\frac{T_n}{T_1})} \quad \text{or} \quad \frac{T_2}{T_1} = \frac{P_2}{P_1}^{\frac{\kappa-1}{\eta_p \kappa}} \tag{1.11}$$

Figure 1.12 illustrates how this definition results in an efficiency than is higher than the isentropic one because, due to the divergence of the iso-pressure lines, $\sum \Delta T^i > T_n^i - T_1$. The use of polytropic efficiency is recommended for multistage compressors because it results in a value of the overall efficiency that is closer to the efficiency of the individual stages.

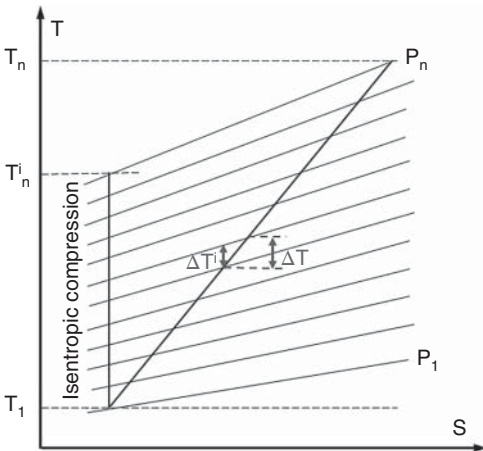


Figure 1.12 Definition of polytropic efficiency.

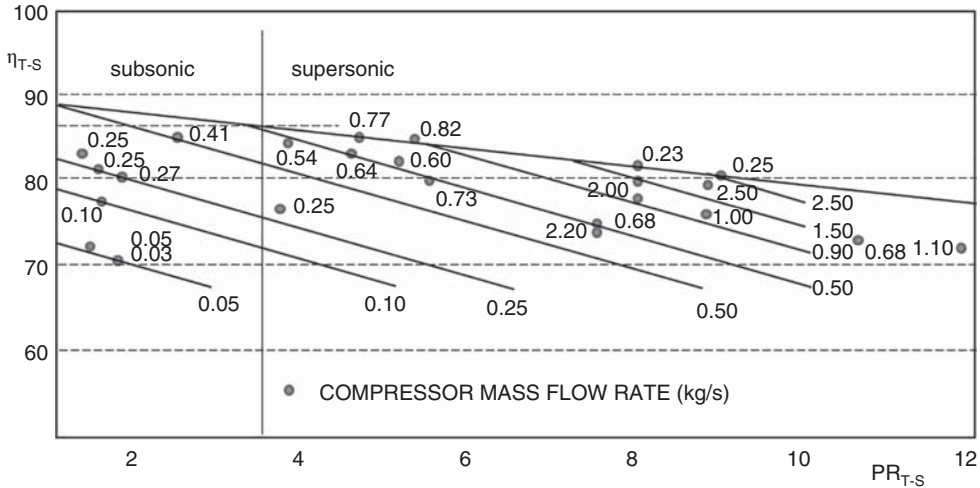


Figure 1.13 Variation of efficiency with pressure ratio and mass flow (from Japikse and Baines 1994).

Figure 1.13 shows an estimation of the achievable total to static efficiency of radial compressors in function of the mass flow and pressure ratio. Black dots indicate experimental data. The number next to them specifies the mass flow in kg/s at which that efficiency has been obtained. The lines on the figure define trends based on average values and may help in estimating the achievable performance of new designs. Very high values of maximum total to static efficiencies (up to 89%) are predicted at low pressure ratio. They are the result of an extrapolation of the high pressure ratio values. They are also not confirmed by experimental data and seem too optimistic.

The trends on Figure 1.13 can be explained by means of a model based on correlations available in the literature. It starts from the maximum impeller efficiency curve corresponding to large compressors operating at high Reynolds number and optimal specific speed (Figure 1.14) (Rodgers 1980). We observe maximum efficiencies that are much higher than the ones on Figure 1.2. This is a consequence of the improved understanding of the flow in radial compressors, obtained from more detailed experimental results (Fowler 1966; Eckardt 1976) and

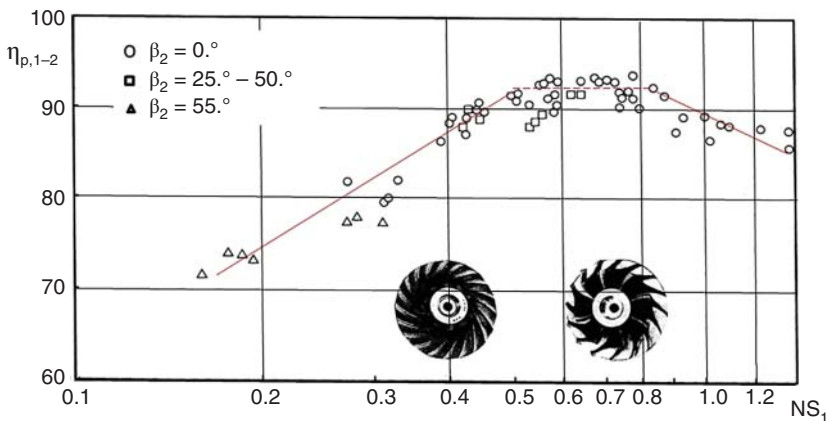


Figure 1.14 Variation of impeller polytropic efficiency ($T-T$) with non-dimensional specific speed (from Rodgers 1980).

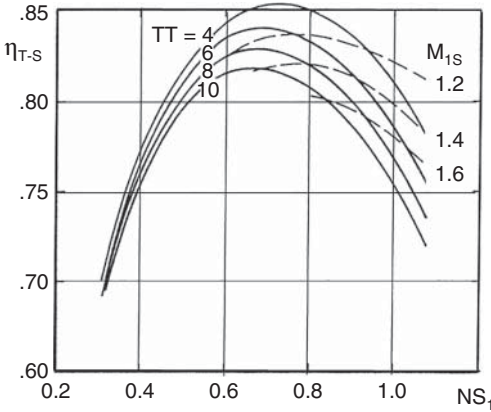


Figure 1.15 Variation of compressor T - S efficiency with non-dimensional specific speed and inlet Mach number (from Rodgers 1991).

full 3D Navier–Stokes analyses that have become possible on modern computers. The top line on this figure fixes the maximum polytropic impeller efficiency at 92%. This is in agreement with a maximum T - S stage efficiency of 86.5% for pressure ratios below 3 on Figure 1.13.

Two corrections to this reference value have to be implemented. The first one accounts for Mach number effects. It results in a decrease in the efficiency for pressure ratios larger than 3, when the impeller inlet flow becomes transonic. This is illustrated in Figure 1.15 and the impact on efficiency is estimated at

$$\Delta\eta_C = \lambda_M(M_{1,S} - 1.0) \quad (1.12)$$

where $\lambda_M = -0.1$ (Rodgers 1991). This explains the interest in designing impellers for minimum relative inlet Mach number at the shroud in order to postpone transonic flows to higher pressure ratios.

The second correction makes use of the Reynolds number to account for the change in efficiency with compressor size and operating conditions:

$$\frac{1 - \eta}{1 - \eta_{ref}} = a + (1 - a) \left(\frac{Re_{b2,ref}}{Re_{b2}} \right)^n \quad (1.13)$$

where η_{ref} corresponds to the efficiency at a known reference Reynolds number $Re_{b2,ref}$, Re_{b2} is the Reynolds number at the operating point, a expresses the fraction of the compressor losses that do not scale with viscosity, such as clearance and leakage losses and therefore independent of Reynolds number, and n is an empirical factor, typically between 0.16 and 0.50, that depends on Reynolds number, roughness, and geometry.

The Reynolds number used in this correlation

$$Re_{b2} = \frac{U_2 b_2}{\mu} \rho_2 \quad (1.14)$$

is based on the impeller outlet width b_2 because $2b_2 \approx DH$, the hydraulic diameter of an impeller flow passage near the exit, where the friction is dominant.

Previous correction accounts only implicitly for the impact of roughness on compressor losses by a change in the exponent n . A more explicit estimation has been proposed by Simon and Bultskamper (1984), Casey (1985), and Strub et al. (1987). They scale the losses by the friction coefficient instead of Reynolds number. This allows more explicit accounting for changes in both viscosity and roughness:

$$\frac{1 - \eta}{1 - \eta_{ref}} = \frac{a + (1 - a)C_f/C_{f,\infty}}{a + (1 - a)C_{f,ref}/C_{f,\infty}} \quad (1.15)$$

C_f is the Darcy friction coefficient, a function of the Reynolds number, wall roughness specified by the equivalent sand grain size k_s , and the hydraulic diameter DH . It is defined by the implicit formula of Colebrook (1939):

$$\frac{1}{\sqrt{C_f}} = -2 \log_{10} \left(\frac{k_s}{3.7DH} + \frac{2.51}{Re \sqrt{C_f}} \right) \quad (1.16)$$

In explicit form it reads:

$$C_f = \frac{0.0625}{\left\{ \log \left[\frac{k_s}{3.7DH} - \frac{5}{Re} \log \left(\frac{k_s}{3.7DH} - \frac{5}{Re} \log \left(\frac{k_s}{3.7DH} \right) \right) \right] \right\}^2} \quad (1.17)$$

$C_{f,\infty}$ is the friction coefficient on hydraulically smooth walls at high Reynolds number. $C_{f,ref}$ is the friction coefficient at the flow conditions at which η_{ref} has been defined.

This relation is shown in Figure 1.16. We observe that an increase in Reynolds number will not result in a decrease in the friction coefficient unless the surface is sufficiently smooth. This figure also shows that smoothing of the surface is useful only if the Reynolds number is larger than a critical value function of the relative roughness. Hence Equation (1.15) allows the impact of a change in the roughness of a given geometry at constant Reynolds number to be evaluated. It turns out that smoothing of the surfaces is useful only if the Reynolds number based on the sand grain size k_s :

$$Re_{k_s} = \frac{U k_s}{\mu} \rho < 100 \quad (1.18)$$

Childs and Noronha (1999) pointed out that the effect of roughness depends on the shape of the roughness, which in turn depends on the manufacturing technique. Casting results in an unstructured sand grain type roughness (Figure 1.17a) whereas machining gives rise to a structured pattern composed of cusp heights and cutter path roughness in between (Figure 1.17b). In the first case the effect of roughness on friction is independent of the flow direction. This is not the case on machined surfaces where an alignment of the machine's cutter path to the flow

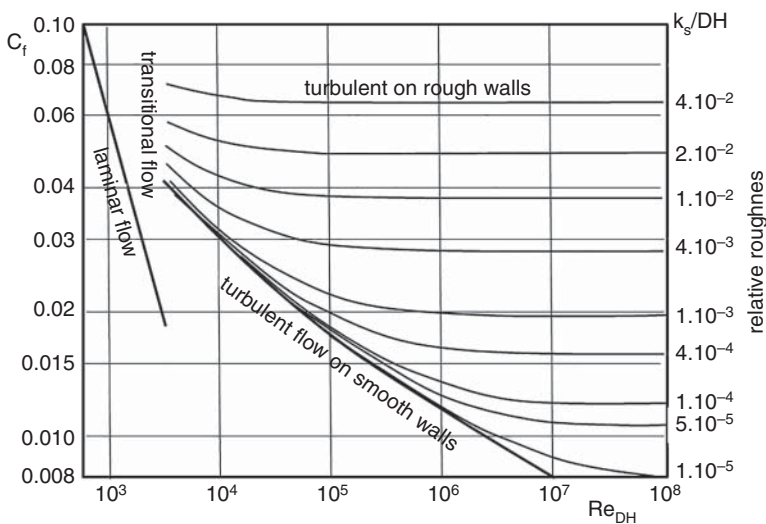


Figure 1.16 Variation of friction coefficient with Reynolds number and roughness (from Strub et al. 1987).

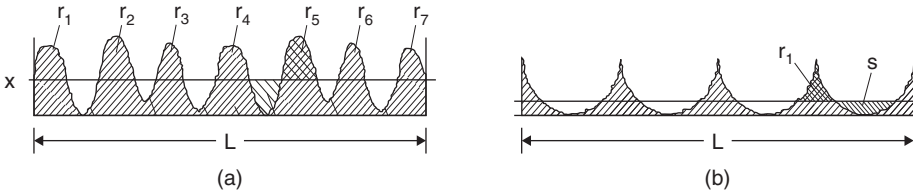


Figure 1.17 Centerline average roughness definition for (a) casted and (b) machined surfaces (from Childs and Noronha 1999).

direction may reduce the apparent roughness to the one inside each cutting path and may even have a favorable effect on the performance by a kind of alignment of the boundary layer to the main flow.

The width of the cusps and cutter path roughness depend on the size of the cutting tool and cutter speed, which in turn have an important impact on manufacturing cost. As stated by Childs and Noronha (1999), cutter marks may also affect the fatigue life of the blades, tend to retain deposits, and accelerate stress corrosion on the substrate metal.

Depending on the geometry, the fraction of viscous losses a in (1.13) and (1.15) at peak efficiency can vary between 0.0 and 0.57 (Wiesner 1979). Casey and Robinson (2011) tried to eliminate this dependence by calculating the change in efficiency directly:

$$\Delta\eta = -B_{ref} \frac{\Delta C_f}{C_{f\infty}} \tag{1.19}$$

This expression is nothing other than Equation (1.15), but written in a different way:

$$\Delta\eta = -\frac{a + (1 - a)}{a + (1 - a)C_{f,ref}/C_{f,\infty}} (1 - \eta_{ref}) \frac{\Delta C_f}{C_{f,\infty}} \tag{1.20}$$

Hence also B_{ref} depends on a and the authors provide a very useful correlation defining B_{ref} as a function of specific speed NS (Figure 1.18):

$$B_{ref} = 0.05 + \frac{0.025}{(NS_1 + 0.2)^3} \tag{1.21}$$

where NS_1 is the specific speed based on the flow at reference conditions.

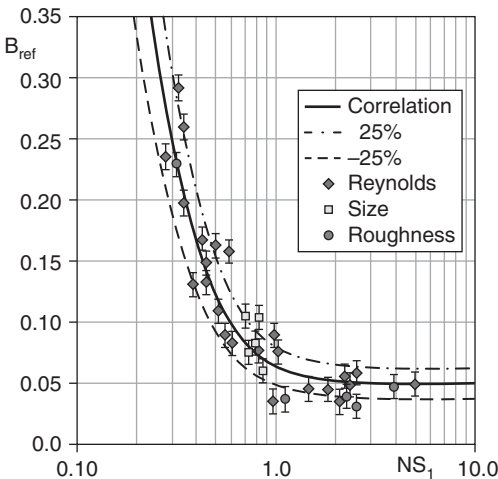


Figure 1.18 Variation of parameter B_{ref} as a function of non-dimensional specific speed (from Casey and Robinson 2011).

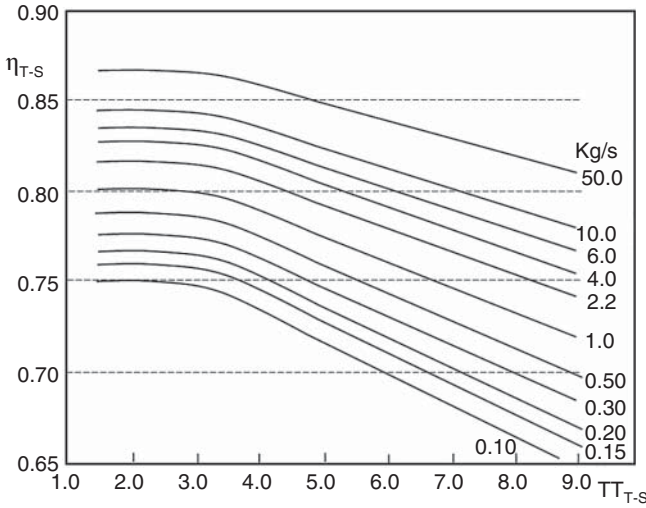


Figure 1.19 Achievable compressor efficiency as a function of pressure ratio and mass flow.

The Mach number effect (Equation (1.12)) defines the change in maximum efficiency as a function of pressure ratio. Combining the correction for Mach number and Reynolds number results in a variation of the maximum achievable efficiency, as shown in Figure 1.19. This figure is based on Equation (1.13) with $a = 0.5$ and $n = 0.9879/Re^{0.24335}$, with atmospheric inlet flow conditions and, strictly speaking, valid only for a change in Reynolds number at unchanged relative roughness $k_s/DH = C^{te}$. The following less relevant definition of the Reynolds number is used because the impeller outlet width may not be known when estimating the maximum efficiency at the early stage of a design,

$$Re = \frac{U_2 R_2}{\mu} \rho_2 \quad (1.22)$$

Re_{ref} is the Reynolds number corresponding to an impeller with 50 kg/s mass flow at atmospheric inlet conditions and sufficiently smooth surfaces to eliminate roughness effects. The upper curve on Figure 1.19 corresponds to such impellers. The surface roughness is assumed to be sufficiently small as to have no influence.

The decrease in efficiency for pressure ratios above three is due to increasing transonic flow losses in the inducer. The decrease in efficiency at a fixed pressure ratio (abscissa) is the consequence of a decreasing Reynolds number with decreasing volume flow or size. The final efficiency may be lower because not all compressors are designed at optimum specific speed and sufficiently small relative roughness and not necessarily for maximum efficiency.

A typical variation of the compressor efficiency curves with Reynolds number is shown in Figure 1.20. The corresponding change in the pressure rise and volume flow curve is similar to the one resulting from a small change in RPM. At unchanged throttle setting the change in volume flow \dot{Q} is defined by:

$$\frac{\dot{Q}}{\dot{Q}_{ref}} = \sqrt{\frac{\Delta H^i}{\Delta H_{ref}^i}} \quad (1.23)$$

ΔH^i is the enthalpy rise corresponding to the pressure rise ΔP . According to Strub et al. (1987) only half of the decrease/increase in efficiency appears as an decrease/increase in isentropic head (ΔH^i) because the change in flow also results in an opposite change (increase/decrease)

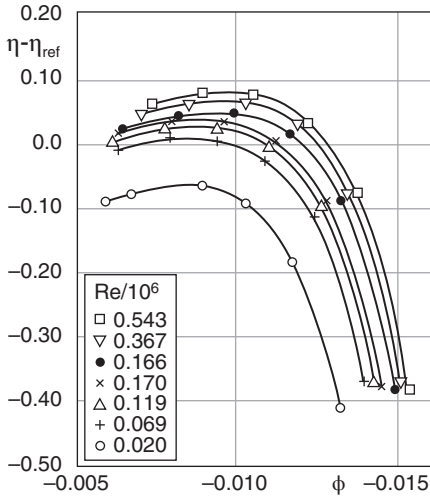


Figure 1.20 Variation of efficiency and volume flow with Reynolds number (from Casey 1985).

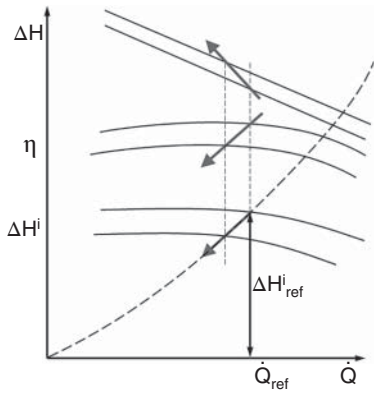


Figure 1.21 Variation of work input and isentropic head with efficiency.

in the work input (ΔH) as defined by the following relations, illustrated in Figure (1.21):

$$\frac{\Delta H^i}{\Delta H_{ref}^i} = 0.5 + 0.5 \frac{\eta}{\eta_{ref}} \tag{1.24}$$

$$\frac{\Delta H}{\Delta H_{ref}} = 0.5 + 0.5 \frac{\eta_{ref}}{\eta} \tag{1.25}$$

1.3 Diabatic Flows

Most compression and expansion processes are treated as adiabatic, neglecting the heat exchange with the external world. However, large amounts of heat transfer may take place in turbochargers and small gas turbines between the hot turbine and colder compressor, and between the compressor impeller and an external shroud. The amount of heat exchange depends on the temperature of the heat source and the geometry. It is largest in an overhang layout where the compressor is next to the turbine (Figure 1.9b). In a more traditional layout with a central bearing (Figure 1.9a) the heat transfer may be smaller and influenced by the oil temperature.

This heat loss in the turbine decreases the amount of available energy in the gas but increases the polytropic efficiency because of a reduction in the reheat effect. The heat addition in the compressor increases the shaft power needed to compress the gas because the compression takes place at a higher temperature. The main consequence of the internal heat transfer is a modification of the operating point of the turbocharger or gas turbine (Van den Braembussche 2005).

A further consequence of an increase in the compressor fluid temperature is a lower gas density at the impeller outlet and hence a reduced diffusion, resulting in a lower pressure rise and a change in the velocity triangles at the diffuser inlet. At unchanged shaft power, the compressor pressure ratio will be lower (Gong et al. 2004). Experimental results by Rautenberg et al. (1983) and Sirakov and Casey (2011), however, indicate that at unchanged pressure ratio more power is needed to drive the compressor. In what follows one will neglect these changes and assume that the velocity is unchanged along a streamline and that the friction losses can be evaluated from the polytropic efficiency of an adiabatic compression.

The measured exit temperatures are no longer representative for the mechanical power consumption of the compressor. They will lead to erroneous values of the efficiency if the non-adiabatic effects are not taken into consideration. Adiabatic efficiencies have to be used when calculating the turbocharger efficiency:

$$\eta_{TC} = \eta_{C,ad} \eta_{T,ad} \eta_{mech} \quad (1.26)$$

The effect of a non-adiabatic compression or expansion is illustrated in Figure 1.22.

Heating the flow during compression has a negative effect on the efficiency because the enthalpy dH needed for an elementary isentropic compression dP increases with temperature:

$$dH = \frac{dP}{\rho} = \frac{dP}{P} R_G T \quad (1.27)$$

Cooling the flow during the expansion in a turbine has also a negative effect on the power output because the energy dH obtained from an isentropic pressure drop dP decreases with decreasing temperature. Neglecting the heat loss may result in an apparent efficiency in excess of 100%.

The second law of thermodynamics provides the relation for non-isentropic diabatic compression (Equation (1.57)):

$$dH = \frac{dP}{\rho} + T dS = \frac{dP}{\rho} + dH_{fr} + dq \quad (1.28)$$

where dH_{fr} is the heat produced by the internal friction losses and dq is the amount of heat per unit mass transmitted through the walls. Distributing the losses and heat addition uniformly

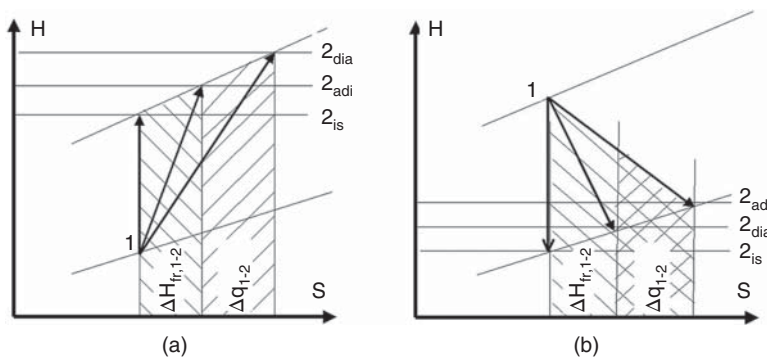


Figure 1.22 H, S diagram for (a) diabatic compression or (b) diabatic expansion.

over the enthalpy rise

$$dH_{fr} = \frac{\Delta H_{fr,1-2}}{H_2 - H_1} dH \qquad dq = \frac{\Delta q_{12}}{H_2 - H_1} dH \qquad (1.29)$$

and substituting it into Equation (1.28) provides the following relation:

$$\left(1 - \frac{\Delta H_{fr,1-2}}{H_2 - H_1} - \frac{\Delta q_{1-2}}{H_2 - H_1} \right) dH = \frac{dP}{\rho} \qquad (1.30)$$

Using the perfect gas relation to calculate the density and expressing the enthalpy as a function of the temperature change and constant specific heat coefficient C_p one obtains

$$\left(1 - \frac{\Delta H_{fr,1-2}}{C_p(T_2 - T_1)} - \frac{\Delta q_{1-2}}{C_p(T_2 - T_1)} \right) dT = \frac{\kappa - 1}{\kappa} T \frac{dP}{P} \qquad (1.31)$$

Integrating this relation from inlet to outlet results in

$$\ln \frac{T_2}{T_1} \left(1 - \frac{\Delta H_{fr,12} + \Delta q_{1-2}}{C_p(T_2 - T_1)} \right) = \frac{\kappa - 1}{\kappa} \ln \frac{P_2}{P_1} \qquad (1.32)$$

or

$$\frac{T_2}{T_1} = \frac{P_2}{P_1}^\mu \qquad \mu = \frac{\frac{\kappa - 1}{\kappa}}{1 - \frac{\Delta H_{fr,1-2} + \Delta q_{1-2}}{C_p(T_2 - T_1)}} \qquad (1.33)$$

This equation is similar to the definition of the polytropic efficiency of an adiabatic compression (Equation (1.11)). Hence

$$\eta_{p,dia} = 1 - \frac{\Delta H_{fr,1-2} + \Delta q_{1-2}}{C_p(T_2 - T_1)} \qquad (1.34)$$

which means that $\eta_{p,dia}$ decreases with positive values of Δq_{1-2} because any heat addition increases both the nominator and denominator of the RHS by the same amount. Similar equations can be derived for turbines.

The variation in compressor efficiency as a function of the adiabatic efficiency and heat flux is shown in Figure 1.23. Δq_{1-2} is non-dimensionalized by the adiabatic compressor energy input at $\eta_p = 0.7$.

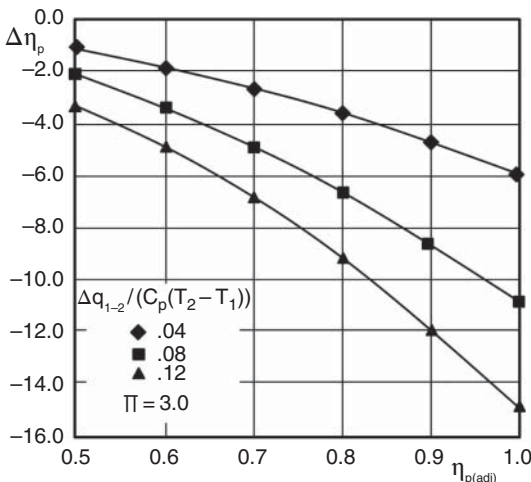


Figure 1.23 Decrease in the compressor polytropic efficiency as a function of adiabatic efficiency for different values of the non-dimensionalized heat flux.

The measured diabatic outlet temperature cannot be directly used to calculate the power absorbed by the compressor or delivered by the turbine. The heat transfer from the turbine to the compressor ($\Delta Q_{1-2} \neq 0$) is required to correctly assess the compressor aerodynamic performance map. The shaft power needed to drive the compressor is obtained by subtracting the heat flux from the total energy transfer, defined from the measured inlet and outlet temperature.

$$Pw_{dia,C} = \dot{m}C_p(T_{2,dia} - T_1) - \Delta Q_{1-2} \quad (1.35)$$

The change in polytropic efficiency depends on the amount of heat that is added (Equation (1.34)). The value of $\Delta H_{fr,1-2}$ can be directly derived from the efficiency of an adiabatic compression ($\Delta Q_{1-2} = 0$):

$$\Delta H_{fr,1-2} = (1 - \eta_{p,ad})C_p(T_{2,ad} - T_1) \quad (1.36)$$

Comparing the adiabatic and diabatic efficiency allows estimation of the amount of heat transfer. Cold tests are not representative for the performance under real operating conditions but comparing the results with a hot test allows the amount of heat flux from the hot parts to the compressor to be assessed.

Measurements by Rautenberg et al. (1983) show the impact of the heat transfer on efficiency in a classical turbocharger geometry with a central bearing (Figure 1.24a) and in an overhang geometry with the compressor close to the hot turbine (Figure 1.24b). Solid lines are for a given amount of heat flux defined by

$$\epsilon_{dia} = \frac{\eta_{ad} - \eta_{dia}}{\eta_{ad}} = \frac{\Delta Q_{1-2}}{\dot{m}(H_2 - H_1)_{dia}} \quad (1.37)$$

As the heat transfer ΔQ_{1-2} depends mainly on the wall temperatures and less on the compressor operating conditions, it is obvious that the impact on efficiency will be largest at low mass flows and low pressure ratios because $(\dot{m}(H_2 - H_1))$ is smaller.

The heat transfer inside a micro gas turbine with central bearing has been numerically evaluated by Verstraete et al. (2007) for a compressor with seven full and seven splitter blades operating at atmospheric inlet conditions and a turbine inlet temperature of 1200 K. The results

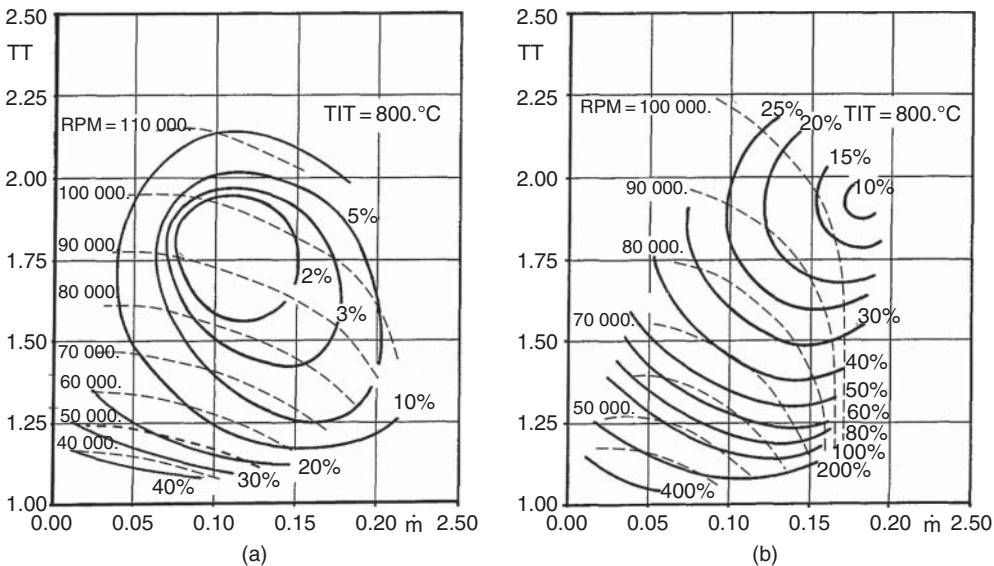


Figure 1.24 Typical heat flux number (a) for a turbocharger with central bearing and (b) for an overhang geometry with the compressor close to the turbine (from Rautenberg et al. 1983).

Table 1.1 Variation of the heat transfer with compressor size, conductivity, and geometry.

	$\lambda = 28 \text{ W/(m.K)}$			Gap in house	$\lambda = 50 \text{ W/(m.K)}$	$Q_{shroud} = 0$
	Geo. 1	Geo. 2	Geo. 3	Geo. 2M	Geo. 2	Geo. 2
2R (mm)	10	20	40	20	20	20
P_w (W)	900	3 570	14 250	3 570	3 570	3 570
\dot{m} (g)	5.37	21.50	86.00	21.50	21.50	21.50
ΔQ_{1-2} (W)	11.6	34.4	124.0	26.0	37.0	76.0
ΔQ_{2-4} (W)	50	140	382	56	160	134
$\Delta \eta_{T-T}$ (%)	1.7	0.7	0.7			3.2

for impeller diameters between 10 and 40 mm with different shapes of bearing house and conductivity of the material are summarized in Table 1.1. All dimensions scale with the impeller diameter. The compressor and turbine shroud wall temperatures are fixed at 300 and 1000 K except for the data in the last column obtained with an adiabatic compressor shroud. The geo. 2M differs from the other by a 2-mm wide cavity in the bearing house to reduced the heat transfer from the hot turbine side to the cooler compressor side (Figure 1.25).

The total amount of heat flux ΔQ_{1-2} transmitted to the compressor fluid by the impeller hub and blades, minus the heat loss through the shroud, varies between 11.60 W for geo. 1 and 124 W for geo. 3. This is the value to be used in Equation (1.34). Only 25 W passes through the shaft of geo. 2 when it is made of the lower conductivity material. This value increases with the cross section (R^2) and decreases with the length L , hence scales with R^1 . The rest of the heat enters through the impeller hub cavity by heat transfer from the bearing wall and by disk friction. The first one is proportional to the surface, hence scales with R^2 . The disk friction losses are proportional to $U_2^3 R_2^2$. Identical pressure ratio in the three geometries requires the same value for U_2 , so that this contribution to the heat transfer scales with R^2 . The predicted values are in line with the experimental ones in Figure 1.24.

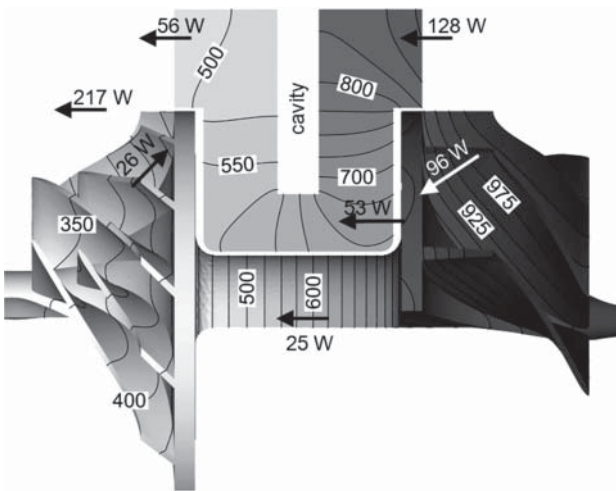


Figure 1.25 Temperature and heat transfer inside a compressor–hot turbine combination with the compressor shroud wall at 300 K (from Verstraete et al. 2007).

Only a small drop in efficiency $\Delta\eta_{T-T}$ is observed when imposing a 300 K wall temperature on the shroud as a consequence of the large heat loss through that wall. Assuming an adiabatic shroud wall for geo. 2 (the last column in Table 1.1), the total amount of heat transmitted to the impeller is transmitted to the fluid, resulting in a much larger efficiency drop (3.2%). The thermal insulation of the compressor shroud wall enhances the impact of the internal heat transfer on efficiency.

A large amount of heat enters the fluid at the vaneless diffuser hub (140 W in geo. 2 and 56 W in geo. 2M). This increases the compressor outlet temperature but has no direct impact on the real compressor efficiency.

A more detailed split of the heat transfer in geo. 2M is shown in Figure 1.25. The imbalance between the heating and cooling of the bearing house shown on this figure is due to the leakage flow transporting heat from the compressor hub cavity to the turbine inlet along the air bearing. The 217 W heat flux on the impeller and diffuser shroud is also partially due to the temperature increase of the fluid during compression.

The impact of the wall temperature on the compressor efficiency has also been studied by Isomura et al. (2001) and Sirakov et al. (2004).

1.4 Transformation of Energy in Radial Compressors

The main dimensions of the impeller and diffuser are defined in Figure 1.26.

The flow entering the impeller has a meridional velocity component V_{m1} and in case of preswirl also a tangential component V_{u1} (Figure 1.27). These velocity components together

Figure 1.26 Definition of geometrical parameters.

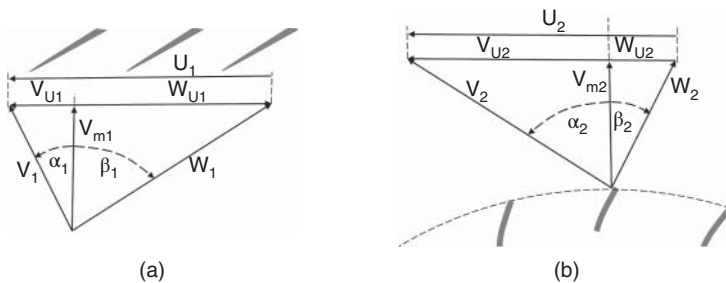
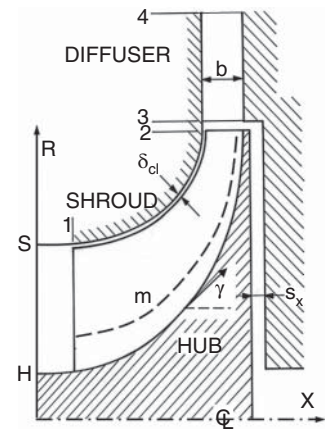


Figure 1.27 Velocity triangle at impeller (a) inlet and (b) outlet.

with the peripheral speed \vec{U}_1 define the velocity triangle at the rotor inlet. The angle convention for the relative flow is:

- $\beta_1 > 0$ is as shown in Figure 1.27a
- $\beta_2 > 0$ for backward leaning blades is as shown in Figure 1.27b. This is a logical choice because it does not require a change of sign for the relative flow angle between inlet and outlet of backward leaning blades.

For forward leaning blades ($\beta_2 < 0$) an obvious position for the change of sign is where the blade becomes radial:

$$\vec{V}_1 = \vec{V}_{u1} + \vec{V}_{m1} \quad (1.38)$$

The spanwise distribution of the inlet axial velocity depends on the shape of the inlet channel. In the case of an axial inlet a uniform axial velocity can be assumed. In the case of a radial to axial inlet section the spanwise variation will depend on the meridional curvature.

The relative velocity and flow angle vary over the blade height at the impeller inlet because of the change in peripheral and eventually axial velocity with radius:

$$\vec{V}_1 = \vec{W}_1 + \vec{U}_1 \quad (1.39)$$

Optimum impeller performance is expected when the relative inlet velocity is nearly parallel to the blade at the leading edge. Mass flow variation around this point is limited by the increasing diffusion or choking losses at positive or negative incidence, respectively.

The absolute velocity at the impeller outlet is defined from the relative outlet velocity \vec{W}_2 and the local circumferential velocity \vec{U}_2 (Figure 1.27b):

$$\vec{V}_2 = \vec{U}_2 + \vec{W}_2 \quad (1.40)$$

In a first approach one assumes that the outlet relative velocity (magnitude and direction) is uniform in the spanwise direction. The large peripheral velocity results in a large absolute velocity and hence large kinetic energy at the diffuser inlet. This energy is then transformed into potential energy (pressure) by decelerating the flow from \vec{V}_2 to the diffuser exit velocity \vec{V}_3 .

The fluid enters the impeller with an angular momentum

$$\int_{R_H}^{R_S} R_1 V_{u1} d\dot{m} \quad (1.41)$$

and leaves the impeller with an angular momentum

$$\int_0^b R_2 V_{u2} d\dot{m} \quad (1.42)$$

The difference results from the forces exerted by the impeller on the fluid. Assuming a spanwise uniform flow at the exit, the equation of angular momentum results in

$$Mo = R_2 V_{u2} \dot{m} - \int_{R_H}^{R_S} R_1 V_{u1} d\dot{m} = \dot{m}(R_2 V_{u2} - \tilde{R}_1 \tilde{V}_{u1}) = \iint R(F_{u,PS} - F_{u,SS}) dS \quad (1.43)$$

where \tilde{R}_1 and \tilde{V}_{u1} are mass averaged values at the rotor inlet. $F_{u,PS}$ and $F_{u,SS}$ are the tangential force components on the suction and pressure side of the blades, respectively.

The energy per unit mass flow transmitted by the impeller *along a streamline* does not require an averaging at the rotor inlet:

$$\frac{\Omega F_u \tilde{R}}{\dot{m}} = \frac{P_w}{\dot{m}} = U_2 V_{u2} - U_1 V_{u1} = \Delta H \quad (1.44)$$

This equation is valid along any streamline for isentropic and non-isentropic flows as well, as long as the flow is adiabatic. Adiabatic must be interpreted here in a strict way, i.e. not only no heat but also no work addition/subtraction from outside the control volume by friction on walls that are moving relative to the rotor (i.e. the fixed shroud in open impellers) (Lyman 1993). A model to estimate this energy dissipation is described by Sikarov et al. (2004). The torque on the shaft contributes to the enthalpy rise of the impeller fluid but part of it is needed to overcome the drag generated by the non-rotating shroud:

$$Pw_{shaft} - \Omega M o_{fr} = \dot{m}(U_2 V_{u2} - \tilde{U}_1 \tilde{V}_{u1}) \quad (1.45)$$

Gong et al. (2004) consider this removal of energy from the rotor fluid as casing drag loss. They have estimated it in the extreme case of a 4-mm diameter micro gas turbine impeller with central bearing at 13% of the total power transmitted by the shaft. Except for the disk friction losses on the impeller backplate this non-adiabatic energy exchange is normally neglected in one-dimensional (1D) prediction methods. In shrouded impellers the shroud drag losses are replaced by disk friction losses on the outer wall of the shroud.

The following relations can be derived from the Figure 1.27:

$$W_1^2 = V_1^2 + U_1^2 - 2U_1 V_{u1} \quad (1.46)$$

$$W_2^2 = V_2^2 + U_2^2 - 2U_2 V_{u2} \quad (1.47)$$

Substituting them in Equation (1.44) one obtains

$$\Delta H = \frac{1}{2}(V_2^2 - V_1^2 + W_1^2 - W_2^2 + U_2^2 - U_1^2) \quad (1.48)$$

This equation is different from the one derived for axial compressors by the term $\frac{1}{2}(U_2^2 - U_1^2)$ and explains why:

- a much larger enthalpy rise can be achieved in radial compressors ($U_2 > U_1$) than in axial ones
- the diffusion from $W_1 \rightarrow W_2$ must be much larger at the shroud than at the hub to obtain the same work input on both sides and as a consequence flow separation is more common at the shroud than at the hub
- radial compressors can be very efficient in spite of an eventual flow separation in the impeller. The diffusion from W_1 to W_2 is only part of the energy transfer in the impeller and the impact of an inefficient deceleration of the relative flow can be minimized by the large extra work input $U_2^2 - U_1^2$.

The same equation can also be derived from the equations of motion and energy. Although its derivation is more complicated, it is also worth looking at because it provides a better physical understanding of the mechanisms of energy transfer and allows a further clarification of the conditions of validity.

The **equation of motion in non-rotating systems** (absolute motion) expresses the equilibrium between the acceleration \vec{a} and:

- the local pressure gradients $\frac{\nabla P}{\rho}$
- the gravity forces/unit mass $\nabla(gz)$
- the friction forces/unit mass \vec{f}_{fr}

$$\vec{a} = -\frac{\nabla P}{\rho} - \nabla(gz) + \vec{f}_{fr} \quad (1.49)$$

whereby the acceleration is the change in velocity along a streamline, defined by:

$$\vec{a} = \frac{DV}{dt} = \frac{\partial V}{\partial t} + \vec{V} \cdot \nabla \vec{V} \tag{1.50}$$

Combining Equations (1.49) and (1.50) for steady flow ($\frac{\partial V}{\partial t} = 0$) provides the equation of motion

$$\vec{V} \cdot \nabla \vec{V} = -\frac{\nabla P}{\rho} - \nabla(gz) + \vec{f}_{fr} \tag{1.51}$$

Making use of the following vector identity (Vavra 1974)

$$\vec{V} \cdot \nabla \vec{V} = \nabla \left(\frac{V^2}{2} \right) - \vec{V} \vee (\nabla \vee \vec{V}) \tag{1.52}$$

it can also be written as:

$$\vec{V} \vee (\nabla \vee \vec{V}) = \frac{\nabla P}{\rho} + \frac{\nabla V^2}{2} + \nabla(gz) - \vec{f}_{fr} \tag{1.53}$$

The **energy equation in the absolute frame of reference** is obtained by integrating the scalar product of the equation of motion (1.51) with a displacement $d\vec{s} = \vec{V} dt$ along a streamline (energy input is force times displacement):

$$\vec{V} \cdot \nabla \vec{V} d\vec{s} = -\frac{\nabla P}{\rho} \cdot d\vec{s} + \vec{f}_{fr} \cdot d\vec{s} - \nabla(gz) \cdot d\vec{s} \tag{1.54}$$

Taking into account that in the absence of heat transfer the entropy increase along a streamline is due only to friction,

$$T \nabla S \vec{V} dt = -\vec{f}_{fr} \cdot \vec{V} dt \tag{1.55}$$

Equation (1.54) can be written as:

$$\left(\nabla \frac{V^2}{2} + \frac{\nabla P}{\rho} + T \nabla S + \nabla(gz) \right) d\vec{s} = 0 \tag{1.56}$$

Considering the second law of thermodynamics, illustrated in Figure 1.28,

$$\frac{\nabla P}{\rho} + T \nabla S = \nabla h \tag{1.57}$$

Equation (1.56) reduces to

$$\left(\nabla \left(h + \frac{V^2}{2} + gz \right) \right) d\vec{s} = 0 \tag{1.58}$$

This equation states that the total enthalpy

$$H = h + \frac{V^2}{2} + gz \tag{1.59}$$

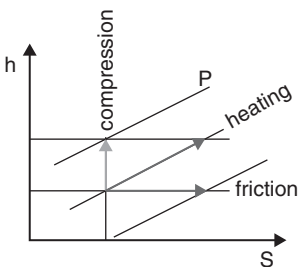


Figure 1.28 Variation of pressure, enthalpy, and entropy.

is constant along a streamline of steady adiabatic flows in the absence of body forces, with or without losses. However, any energy addition by friction on a moving wall violates the adiabatic condition.

Substituting Equation (1.57) into (1.53) results in

$$\vec{V} \cdot \nabla (\nabla \cdot \vec{V}) = \nabla \cdot \left(h + \frac{V^2}{2} + gz \right) - T \nabla S - \vec{f}_f \quad (1.60)$$

Although in adiabatic flows the local entropy increase along a streamline is due to friction (Equation (1.55)), this does not mean that the local entropy gradient $T \nabla S$ is everywhere equal to the local friction forces. The entropy can be different from streamline to streamline depending on the friction forces on the upstream flow path. Hence the last two terms of Equation (1.60) do not cancel.

Isentropic ($\nabla S = 0$), hence frictionless ($\vec{f}_f = 0$), and adiabatic flows with uniform H over the inlet section have constant H over the whole flow field according to Equation (1.59) and are called Beltrami flows. For absolute flows Equation (1.53) then reduces to

$$\vec{V} \cdot \nabla (\nabla \cdot \vec{V}) = 0 \quad (1.61)$$

This equation is satisfied if $\vec{V} = 0$, or \vec{V} is parallel to $(\nabla \cdot \vec{V})$ or when the curl

$$\nabla \cdot \vec{V} = 0 \quad (1.62)$$

The first condition corresponds to a trivial solution and the second one requests that the velocity is parallel to its curl. Hence only Equation (1.62) is a relevant condition.

Two additional accelerations must be added to Equation (1.50) to obtain the **equation of motion for relative flows**:

- one corresponding to the centrifugal force $\vec{a}_{ce} = \vec{\Omega} \cdot \nabla (\vec{\Omega} \cdot \vec{R}) = \Omega^2 \vec{R}$
- one corresponding to the Coriolis force $a_{Co} = 2 (\vec{\Omega} \cdot \vec{W})$.

Hence the acceleration is

$$\vec{a} = \frac{D\vec{V}}{Dt} = \frac{\partial \vec{W}}{\partial t} + \vec{W} \cdot \nabla \vec{W} + 2(\vec{\Omega} \cdot \vec{W}) + \Omega^2 \vec{R} \quad (1.63)$$

$\frac{\partial \vec{W}}{\partial t} = 0$ in steady relative flows (i.e. flows in a rotor at constant RPM with no inlet or outlet circumferential distortions other than the ones rotating with the rotor).

Combining Equations (1.49) and (1.63) results in the following equation of motion for the steady relative flow:

$$\vec{W} \cdot \nabla \vec{W} + 2(\vec{\Omega} \cdot \vec{W}) + \Omega^2 \vec{R} = -\frac{\nabla P}{\rho} + \vec{f}_f - \nabla gz \quad (1.64)$$

Substituting again the vector identity Equation (1.52) but for the relative velocity W one obtains

$$\vec{W} \cdot \nabla (\nabla \cdot \vec{W}) + 2\vec{\Omega} \cdot \vec{W} = \frac{\nabla P}{\rho} - \Omega^2 \vec{R} + \frac{\nabla W^2}{2} - \vec{f}_f + \nabla gz \quad (1.65)$$

The corresponding **energy equation for relative flows** is obtained by integrating Equation (1.64) along a relative streamline starting at the impeller inlet. Considering that $d\vec{s} = \vec{W} \cdot dt$ and everywhere perpendicular to the Coriolis force $\vec{\Omega} \cdot \vec{W}$ (Figure 1.29) the integral of the second term is identical to zero:

$$\int_1 2(\vec{\Omega} \cdot \vec{W}) \vec{W} dt \equiv 0 \quad (1.66)$$

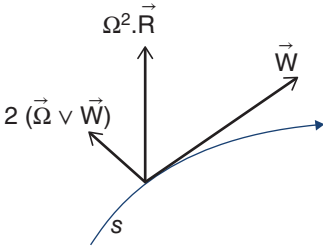


Figure 1.29 Forces in the relative plane.

The integrated value of the centrifugal term is:

$$-\int_1 \Omega^2 \vec{R} dR = -\frac{1}{2}(U^2 - U_1^2) \quad (1.67)$$

The other terms are unchanged so that with Equations (1.55) and (1.56), and after replacing V by W in Equation (1.58) one obtains

$$h + \frac{W^2}{2} - \frac{U^2}{2} + gz = h_1 + \frac{W_1^2}{2} - \frac{U_1^2}{2} + gz_1 = C^{te} = Ro \quad (1.68)$$

In analogy with the total enthalpy, one can commonly define rothalpy Ro for rotating systems which, according to Equation (1.68), is constant along a streamline in an adiabatic rotating system. One should keep in mind that the rothalpy is different from the relative total enthalpy defined by $H_r = h + \frac{\vec{W}^2}{2}$.

As explained in more detail in Lyman (1993), $Ro = C^{te}$ is valid for steady adiabatic flow (with or without friction) along a streamline in a rotor at constant RPM, in absence of body forces. Adiabatic must again be considered in the most strict way: "without energy transfer by friction forces on the non-rotating walls". Equation (1.68) is very useful to estimate local flow conditions inside an impeller.

Considering the second law of thermodynamics Equation (1.57) and substituting constant rothalpy into Equation (1.65) one obtains the following equation of motion, again for isentropic and frictionless flows with constant rothalpy at the inlet (Beltrami flows):

$$\vec{W} \times (\nabla \times \vec{W} + 2\vec{\Omega}) = 0 \quad (1.69)$$

In the case of prerotation, rothalpy relates to total enthalpy at the inlet by

$$Ro_1 = H_1 + \Omega R V_{u1} \quad (1.70)$$

Hence spanwise constant total enthalpy at the inlet corresponds to constant rothalpy only in the case of a free vortex swirl distribution ($RV_{u1} = C^{te}$).

Equation (1.69) is satisfied if $\vec{W} = 0$, \vec{W} parallel to $(\nabla \times \vec{W} + 2\vec{\Omega})$ or when the curl

$$\nabla \times \vec{W} = -2\vec{\Omega} \quad (1.71)$$

The first condition is trivial and the second one requests that the velocity is parallel to its curl. Hence only Equation (1.71) is relevant.

In what follows the gravity terms are neglected because they are irrelevant for gas flows. The total enthalpy by definition being $H = h + V^2$, constant Ro along a streamline (Equation (1.68)) results in the following expression for the enthalpy change between the inlet and the outlet of an impeller:

$$\Delta H = H_2 - H_1 = \frac{1}{2}(V_2^2 - V_1^2 + W_1^2 - W_2^2 + U_2^2 - U_1^2) \quad (1.72)$$

which is identical to Equation (1.48). For non-rotating systems ($U = 0$ and $W = V$) Equation (1.72) reduces to $H_2 = H_1$ as specified in Equation (1.59).

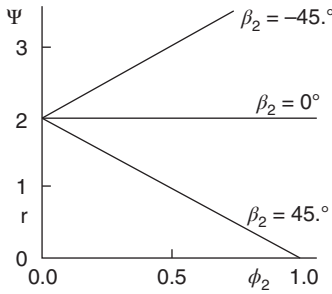


Figure 1.31 Theoretical impeller performance variation for an infinite number of blades.

$$\phi_2 = \frac{\dot{m}}{2\pi R_2 b_2 \rho_2 U_2} = \frac{V_{m2}}{U_2} \tag{1.77}$$

The inlet meridional velocity is linked to the outlet one V_{m2} by continuity. In the absence of compressibility effects (low Mach number flow) it scales with the outlet meridional velocity. The inlet peripheral velocity scales with the outlet peripheral velocity. When operating at different RPM but at the same ϕ and ψ , the inlet and outlet flow angles are conserved and hence also the impeller incidence and diffuser inlet absolute flow angle. Neglecting further the effect of a change in Reynolds number one can conclude that the efficiency will also be unchanged.

The non-dimensionalized parameters ϕ and ψ are useful to define the performance in similar operating points when scaling up or down the geometry or changing rotational speed. The velocity components at the impeller inlet and outlet, corresponding to a given RPM or scale factor, are readily obtained by multiplying ψ and ϕ , respectively, by the corresponding value of U_1^2 and U_2 .

Dividing all terms in Equation (1.74) by $U_2^2/2$, one obtains

$$\psi^\infty = 2(1 - \phi_2 \tan \beta_{2,bl}) \tag{1.78}$$

This relation is plotted in Figure 1.31 for different values of $\beta_{2,bl}$.

Forward leaning blades ($\beta_{2,bl} < 0$) are normally used only for ventilators in air-conditioning systems (squirrel-cage fans). The increasing work input with increasing mass flow compensates for the increase in friction losses in the ducts of the air conditioning system ($\approx \phi^2$). This type of impeller is not used for high pressure ratio compressors because of stability problems.

Radial blades have lower bending stresses and allow higher RPM. They are used for very high pressure ratio compressors and the work input is independent of volume flow.

Backward leaning blades ($\beta_{2,bl} > 0$) show a more stable operation over a large mass flow range at nearly constant power input. They were traditionally used for industrial compressors running at moderate RPM. However, the increased reliability of the stress predictions allows the stress levels to be controlled and the geometry can be adapted accordingly. Backward leaning blades are now commonly used, including in impellers running at large peripheral speeds.

1.5.2 Finite Number of Blades

Previous performance curves are for flows that are parallel to the blades, which is hypothetical as this would require an infinite number of blades. We must correct the curves on Figure 1.31 for real flow effects to find the real enthalpy rise and what part of it is transformed into pressure.

Similar to what is called the deviation in axial compressors, the flow direction at the trailing edge is influenced by the blade shape and viscous effects, including an eventual flow separation in the impeller. This deviation is larger in radial impellers than in axial ones because it is enhanced by the rotationality of the flow resulting from the Coriolis forces.

The impact of this difference in flow direction on the work input is quantified by the work reduction factor, commonly called the slip factor:

$$\mu = \frac{\Delta H}{\Delta H^\infty} \quad (1.79)$$

Its value is normally obtained from empirical correlations. The following theoretical evaluation of μ is due to Stodola (1924) and is theoretically valid only for Beltrami flows.

As will be demonstrated in Section 3.1.2, Equation (1.71) defines the suction to pressure side velocity difference as a function of the blade curvature and impeller rotation. Assuming a straight two-dimensional (2D) rotating channel with incompressible flow and zero blade thickness the suction to pressure side velocity difference (Equation (3.18)) reduces to

$$\frac{W_{SS} - W_{PS}}{h_b} = 2\Omega \quad (1.80)$$

where h_b is the distance from suction to pressure side normal to the streamlines (Figure 1.32). Hence the velocity on the suction side W_{SS} and pressure side W_{PS} can be calculated as a function of a mean velocity \widetilde{W} and the passage vortex -2Ω :

$$W_{SS} = \widetilde{W} + 2\Omega \frac{h_b}{2} \quad W_{PS} = \widetilde{W} - 2\Omega \frac{h_b}{2} \quad (1.81)$$

This passage vortex is at the origin of the slip factor. Stodola (1924) assumed that ΔW_{u2} is equal to the mean value of the tangential velocity component created by the passage vortex in the trailing edge plane (Figure 1.32). Hence

$$\Delta \widetilde{W}_{u2} = 2\Omega \frac{h_b}{2} \times 0.5 \quad (1.82)$$

The impact of this change in tangential velocity (Figure 1.33) on the work input or enthalpy rise is calculated from the Euler momentum equation:

$$\mu = 1 - \frac{\Delta V_{u2}}{V_{u2}^\infty} = 1 - \frac{\Delta W_{u2}}{V_{u2}^\infty} \quad (1.83)$$

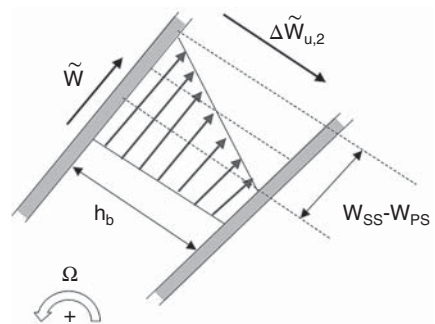
where $\Delta V_{u2} = V_{u2}^\infty - V_{u2}$ and $\Delta W_{u2} = W_{u2} - W_{u2}^\infty$.

This definition of the slip factor is common in German literature (Minderleistungsfaktor) and in what follows it is called the work reduction factor.

Another parameter that characterizes the impact of the vorticity on the outlet flow relates the change in tangential velocity to the peripheral velocity:

$$\sigma = 1 - \frac{\Delta V_{u2}}{U_2} = 1 - \frac{\Delta W_{u2}}{U_2} \quad (1.84)$$

Figure 1.32 Variation of the velocity from suction to pressure side in a straight rotating channel.



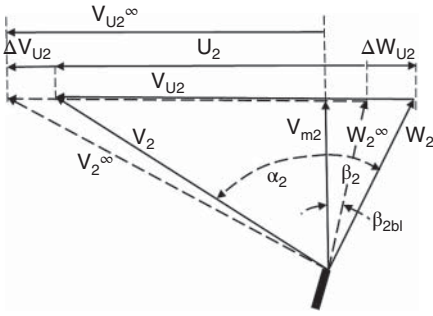


Figure 1.33 Impeller exit velocity triangles with and without slip.

This definition is common in American literature (Wiesner 1967) and in what follows is called the slip factor. Both definitions are identical for compressors with radial ending blades when $V_{u2}^{\infty} = U_2$.

The channel height at the impeller exit h_b can be approximated by

$$h_b = \frac{2\pi R_2 \cos \beta_{2,bl}}{Z_r} \quad (1.85)$$

where Z_r is the number of rotor blades, so that (Figure 1.33)

$$\Delta W_{u2} = \frac{U_2 \pi \cos \beta_{2,bl}}{Z_r} \quad (1.86)$$

From the definition of ψ^{∞} (Equation (1.76)) one has

$$V_{u2}^{\infty} = \frac{\psi^{\infty} U_2}{2} \quad (1.87)$$

After substituting Equations (1.86) and (1.87) into Equation (1.83) one obtains the following expression for the work reduction factor:

$$\mu = 1 - \frac{2\pi \cos \beta_2}{Z_r \psi^{\infty}} \quad (1.88)$$

which relates the hypothetical work coefficient, corresponding to an infinite number of blades ψ^{∞} , to ψ , the real work input taking into account the limited number of blades.

μ is independent of ϕ and the work reduction

$$\Delta \psi_{\mu} = \psi^{\infty} (\mu - 1) = \frac{-2\pi \cos \beta_2}{Z_r} \quad (1.89)$$

is independent of the flow coefficients. The work reduction $\Delta \psi_{\mu}$ is not a loss but quantifies an amount of energy that is not added to the fluid. The corresponding shift of the performance curve is shown in Figure 1.34.

The power to drive the compressor is given by

$$P_w = \Delta H \dot{m} = \psi \phi_2 \pi R_2 b_2 \rho_2 U_2^3 \quad (1.90)$$

1.5.3 Real Performance Curve

The real performance curve for a finite number of blades differs from the one described previously because of a decrease in pressure rise due to losses, as there are friction losses, incidence losses, etc.

Friction losses are proportional to W^2 , or $\Delta \psi_{fr} \approx C_{fr} \phi^2$ where C_{fr} is a friction loss coefficient depending on the geometry, Reynolds number, etc.